

# Interrogating theoretical models of neural computation with deep learning

Sean R. Bittner, Agostina Palmigiano, Alex T. Piet, Chunyu A. Duan, Francesca Mastrogiovanni, Srdjan Ostojic, Carlos D. Brody, Kenneth D. Miller, and John P. Cunningham.

## <sup>1</sup> 1 Abstract

<sup>2</sup> The cornerstone of theoretical neuroscience is the circuit model: a system of equations that captures  
<sup>3</sup> a hypothesized neural mechanism of scientific importance. Such models are valuable when they give  
<sup>4</sup> rise to an experimentally observed phenomenon – whether behavioral or in terms of neural activity –  
<sup>5</sup> and thus can offer insight into neural computation. The operation of these circuits, like all models,  
<sup>6</sup> critically depends on the choices of model parameters. Historically, the gold standard has been  
<sup>7</sup> to analytically derive the relationship between model parameters and computational properties.  
<sup>8</sup> However, this enterprise quickly becomes infeasible as biologically realistic constraints are included  
<sup>9</sup> into the model, often resulting in *ad hoc* approaches to understanding the relationship between  
<sup>10</sup> model and computation. We bring recent machine learning techniques – the use of deep generative  
<sup>11</sup> models for probabilistic inference – to bear on this problem, learning distributions of parameters  
<sup>12</sup> that produce the specified properties of computation. Importantly, the techniques we introduce offer  
<sup>13</sup> a principled means to understand the implications of model parameter choices on computational  
<sup>14</sup> properties of interest. We motivate this methodology with a worked example analyzing sensitivity in  
<sup>15</sup> the stomatogastric ganglion. We then use it to generate insights into neuron-type input-responsivity  
<sup>16</sup> in a model of primary visual cortex, a new understanding of rapid task switching in superior  
<sup>17</sup> colliculus models, and attribution of bias in recurrent neural networks solving a toy mathematical  
<sup>18</sup> problem. More generally, this work suggests a departure from realism vs tractability considerations  
<sup>19</sup> towards the use of modern machine learning for sophisticated interrogation of biologically relevant  
<sup>20</sup> models.

## <sup>21</sup> 2 Introduction

<sup>22</sup> The fundamental practice of theoretical neuroscience is to use a mathematical model to understand  
<sup>23</sup> neural computation, whether that computation enables perception, action, or some intermediate  
<sup>24</sup> processing [1]. In this field, a neural computation is systematized with a set of equations – the  
<sup>25</sup> model – and these equations are motivated by biophysics, neurophysiology, and other conceptual  
<sup>26</sup> considerations. The function of this system is governed by the choice of model parameters, which

27 when configured appropriately, give rise to a measurable signature of a computation. The work of  
28 analyzing a model then becomes the inverse problem: given a computation of interest, how can we  
29 reason about these suitable parameter configurations – their likely values, their uniquenesses and  
30 degeneracies, their attractor states and phase transitions, and more?

31 Consider the idealized practice: a theorist considers a model carefully and analytically derives how  
32 model parameters govern the computation. Seminal examples of this gold standard include our  
33 field’s understanding of memory capacity in associative neural networks [2], chaos and autocorrela-  
34 tion timescales in random neural networks [3], and the paradoxical effect in excitatory/inhibitory  
35 networks [4]. Unfortunately, as circuit models include more biological realism, theory via analytic  
36 derivation becomes intractable. This fact creates an unfavorable tradeoff for the theorist. On the  
37 one hand, one may tractably analyze systems of equations with unrealistic assumptions (for ex-  
38 ample symmetry or gaussianity), producing accurate inferences about parameters of a too-simple  
39 model. On the other hand, one may choose a more biologically relevant model at the cost of *ad hoc*  
40 approaches to analysis (simply examining simulated activity), producing questionable or partial  
41 inferences about parameters of an appropriately complex, scientifically relevant model.

42 Of course, this same tradeoff has been confronted in many scientific fields and engineering problems  
43 characterized by the need to do inference in complex models. In response, the machine learning  
44 community has made remarkable progress in recent years, via the use of deep neural networks as a  
45 powerful inference engine: a flexible function family that can map observed phenomena (in this case  
46 the measurable signal of some computation) back to probability distributions quantifying the likely  
47 parameter configurations. One celebrated example of this approach from the machine learning  
48 community, from which we draw key inspiration for this work, is the variational autoencoder [5, 6],  
49 which uses a deep neural network to induce an (approximate) posterior distribution on hidden  
50 variables in a latent variable model, given data. Indeed, these tools have been used to great success  
51 in neuroscience as well, in particular for interrogating parameters (sometimes treated as hidden  
52 states) in models of both cortical population activity [7, 8, 9, 10] and animal behavior [11, 12, 13].  
53 These works have used deep neural networks to expand the expressivity and accuracy of statistical  
54 models of neural data [14].

55 However, these inference tools have not significantly influenced the study of theoretical neuroscience  
56 models, for at least three reasons. First, at a practical level, the nonlinearities and dynamics of  
57 many theoretical models are such that conventional inference tools typically produce a narrow set  
58 of insights into these models. Indeed, only in the last few years has the deep learning toolkit

59 expanded to a point of relevance to this class of problem. Second, the object of interest from a  
60 theoretical model is not typically data itself, but rather a qualitative phenomenon – inspection of  
61 model behavior, or better, a measurable signature of some computation – an *emergent property* of  
62 the model. Third, because theoreticians work carefully to construct a model that has biological  
63 relevance, such a model as a result often does not fit cleanly into the framing of a statistical model.  
64 Technically, because many such models stipulate a noisy system of differential equations that can  
65 only be sampled or realized through forward simulation, they lack the explicit likelihood and priors  
66 central to the probabilistic modeling toolkit.

67 To address these three challenges, we developed an inference methodology – ‘emergent property  
68 inference’ – which learns a distribution over parameter configurations in a theoretical model. Crit-  
69 ically, this distribution is such that draws from the distribution (parameter configurations) corre-  
70 spond to systems of equations that give rise to a specified emergent property. First, we stipulate a  
71 bijective deep neural network that induces a flexible family of probability distributions over model  
72 parameterizations with a probability density we can calculate [15, 16, 17]. Second, we quantify  
73 the notion of emergent properties as a set of moment constraints on datasets generated by the  
74 model. Thus, an emergent property is not a single data realization, but a phenomenon or a fea-  
75 ture of the model, which is the central object of interest to the theorist (unlike say the statistical  
76 neuroscientist). Conditioning on an emergent property requires an extension of deep probabilistic  
77 inference methods, which we have produced [18]. Third, because we cannot assume the theoretical  
78 model has explicit likelihood on data or the emergent property of interest, we use stochastic gradi-  
79 ent techniques in the spirit of likelihood free variational inference [19]. Taken together, emergent  
80 property inference (EPI) provides a methodology for inferring and then reasoning about parameter  
81 configurations that give rise to particular emergent phenomena in theoretical models.

82 Equipped with this methodology, we investigated three models of current importance in theoretical  
83 neuroscience. These models were chosen to demonstrate generality through ranges of biological  
84 realism (conductance-based biophysics to recurrent neural networks), neural system function (pat-  
85 tern generation to abstract cognitive function), and network scale (four to infinite neurons). First,  
86 to motivate the contribution of emergent property inference, we investigated network syncing in  
87 a classic model of the stomatogastric ganglion [20]. Second, we generated then evaluated a set  
88 of verifiable hypotheses of input-responsivity in a four neuron-type dynamical model of primary  
89 visual cortex. Third, we demonstrated how the systematic application of EPI to levels of task  
90 performance can generate experimentally testable hypotheses regarding connectivity in superior

91 colliculus. Fourth, we leveraged the flexibility of EPI to uncover the sources of bias in a low-rank  
92 recurrent neural network executing a toy computation. The novel scientific insights offered by EPI  
93 contextualize and clarify the previous studies exploring these models [20, 21, 22, 23] and more  
94 generally offer a quantitative grounding for theoretical models going forward, pointing a way to  
95 how rigorous statistical inference can enhance theoretical neuroscience at large.

96 We note that, during our preparation and early presentation of this work [24, 25], another work  
97 has arisen with broadly similar goals: bringing statistical inference to mechanistic models of neural  
98 circuits [26]. We are excited by this broad problem being recognized by the community, and we  
99 emphasize that these works offer complementary neuroscientific contributions and use different  
100 technical methodologies. Scientifically, our work has focused primarily on systems-level theoretical  
101 models, while their focus has been on lower-level cellular models. Secondly, there are several key  
102 technical differences in the approaches (see Section A.1.4) perhaps most notably is our focus on  
103 the emergent property – the measurable signal of the computation in question, vs their focus  
104 on observed datasets; both certainly are worthy pursuits. The existence of these complementary  
105 methodologies emphasizes the increased importance and timeliness of both works.

## 106 3 Results

### 107 3.1 Motivating emergent property inference of theoretical models

108 Consideration of the typical workflow of theoretical modeling clarifies the need for emergent prop-  
109 erty inference. First, the theorist designs or chooses an existing model that, it is hypothesized,  
110 captures the computation of interest. To ground this process in a well-known example, consider  
111 the stomatogastric ganglion (STG) of crustaceans, a small neural circuit which generates multiple  
112 rhythmic muscle activation patterns for digestion [27]. A model of the STG [20] is shown schemat-  
113 ically in Figure 1A, and note that the behavior of this model will be critically dependent on its  
114 parameterization – the choices of conductance parameters  $z = [g_{el}, g_{synA}]$ . Specifically, the two  
115 fast neurons ( $f_1$  and  $f_2$ ) mutually inhibit one another, and oscillate at a faster frequency than  
116 the mutually inhibiting slow neurons ( $s_1$  and  $s_2$ ), and the hub neuron (hub) couples with the fast  
117 or slow population or both. Second, once the model is selected, the theorist defines the emergent  
118 property, the measurable signal of scientific interest. To continue our running STG example, one  
119 such emergent property is the phenomenon of *network syncing* – in certain parameter regimes, the  
120 frequency of the hub neuron matches that of the fast and slow populations at an intermediate fre-

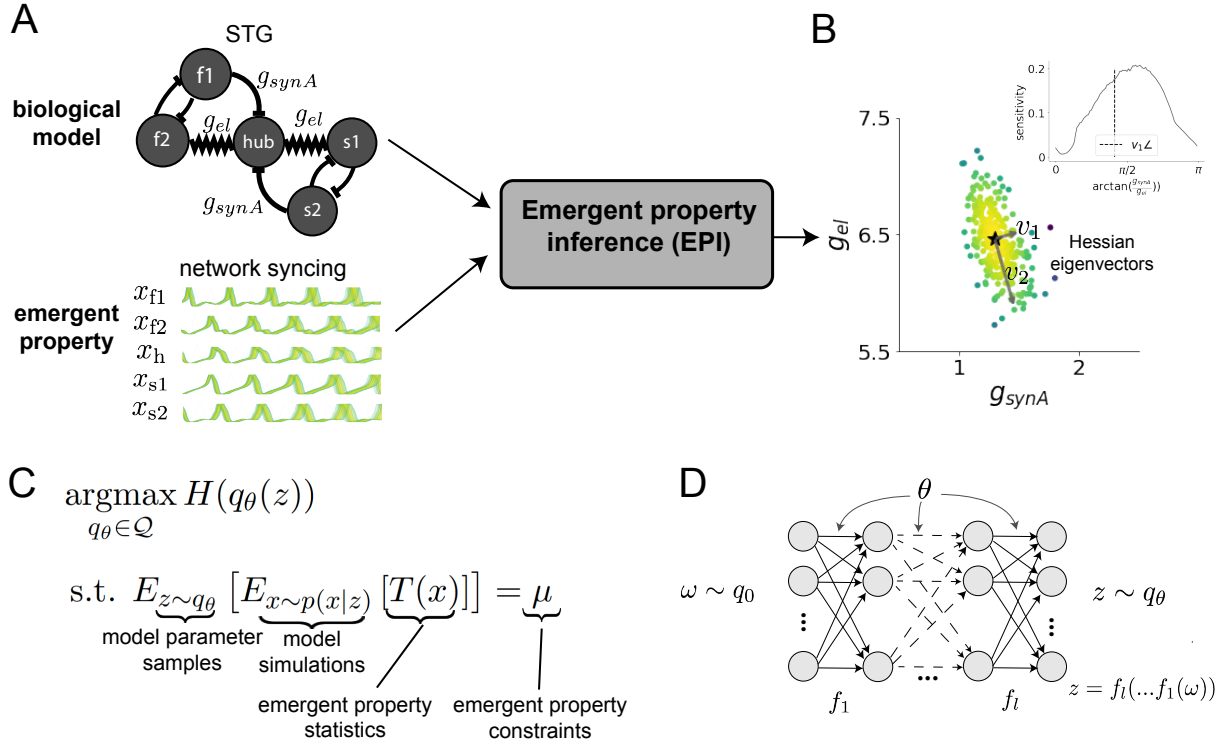


Figure 1: Emergent property inference (EPI) in the stomatogastric ganglion. A. For a choice of model (STG) and emergent property (network syncing), emergent property inference (EPI) learns a posterior distribution of the model parameters  $z = [g_{el}, g_{synA}]^\top$  conditioned on network syncing. B. An EPI distribution of STG model parameters producing network syncing. The eigenvectors of the Hessian at the mode of the inferred distribution are indicated as  $v_1$  and  $v_2$ . (Inset) Sensitivity of the system with respect to network syncing along all dimensions of parameter space away from the mode. (see Section A.2.1). C. EPI learns a distribution  $q_\theta(z)$  of model parameters that produce an emergent property: the emergent property statistics  $T(x)$  are fixed in expectation over parameter distribution samples  $z \sim q_\theta(z)$  to particular values  $\mu$ . EPI distributions maximize randomness via entropy, although other measures are sensible. D. Deep probability distributions map a latent random variable  $\omega \sim q_0$ , where  $q_0$  is chosen to be simple distribution such as an isotropic gaussian, through a highly expressive function family  $f_\theta(\omega) = f_l(\dots f_1(\omega))$  parameterized by the neural network weights and biases  $\theta \in \Theta$ . This mapping induces an implicit probability model  $q(g_\theta(\omega)) \in \mathcal{Q}$

quency. This emergent property is shown in Figure 1A at a frequency of 0.55Hz. Third, qualitative parameter analysis ensues: since precise mathematical analysis is intractable in this model, a brute force sweep of parameters is done. Subsequently, a qualitative description is formulated to describe of the different parameter configurations that lead to the emergent property. In this last step lies the opportunity for a precise quantification of the emergent property as a statistical feature of the model. Equipped with this methodology, we can infer a probability distribution over parameter configurations that produce this quantified emergent property.

Before presenting technical details (in the following section), let us understand emergent property inference schematically: the black box in Figure 1A takes, as input, the model and the specified emergent property, and produces as output the parameter distribution shown in Figure 1B. This distribution – represented for clarity as samples from the distribution – is then a scientifically meaningful and mathematically tractable object. It conveys parameter regions critical to the emergent property, directions in parameter space that will be invariant (or not) to that property. In the STG model, this distribution can be specifically queried to determine the prototypical parameter configuration for network syncing (the mode; Figure 1B star), and then how quickly network syncing will decay based on changes away that mode (Figure 1B, inset). While it is impossible to determine whether we have converged to the maximum entropy distribution, the emergent property statistics have converged to the emergent property values. For further validation, we apply EPI to condition a two-dimensional linear dynamical system model on a band of oscillations around 1Hz, from which we can analytically derive the contours of the inferred distribution (see Section A.1.1). Taken together, bringing careful inference to theoretical models offers deeper insight into the behavior of these models, and the opportunity to make rigorous this last step in the practice of theoretical neuroscience.

### 3.2 A deep generative modeling approach to emergent property inference

Emergent property inference (EPI) systematizes the three-step procedure of the previous section. First, we consider the model as a coupled set of differential (and potentially stochastic) equations [20]. In the running STG example, the dynamical state  $x = [x_{f1}, x_{f2}, x_{hub}, x_{s1}, x_{s2}]$  is the membrane potential for each neuron, which evolves according to the biophysical conductance-based equation:

$$C_m \frac{\partial x}{\partial t} = -h(x; z) = -[h_{leak}(x; z) + h_{Ca}(x; z) + h_K(x; z) + h_{hyp}(x; z) + h_{elec}(x; z) + h_{syn}(x; z)] \quad (1)$$

where  $C_m = 1\text{nF}$ , and  $h_{\text{leak}}$ ,  $h_{Ca}$ ,  $h_K$ ,  $h_{\text{hyp}}$ ,  $h_{\text{elec}}$ ,  $h_{\text{syn}}$  are the leak, calcium, potassium, hyperpolarization, electrical, and synaptic currents, all of which have their own complicated dependence on  $x$  and  $z = [g_{\text{el}}, g_{\text{synA}}]$  (see Section A.2.1).

Second, we define the emergent property, which as above is network syncing: the phase locking of the population and its oscillation at an intermediate frequency of our choosing (Figure 1A bottom). Quantifying this phenomenon is straightforward: we define network syncing to be that the spiking frequency of each neuron is close to an intermediate frequency of 0.55Hz. Thus, our measurable signature of computation – the firing frequencies of each neuron  $\omega_{f1}(x)$ ,  $\omega_{f2}(x)$ , etc.– are statistics of the membrane potential activity  $x$  which we insist be near a particular value 0.55Hz. Mathematically, we achieve this via constraints on the mean and variance of  $\omega_i(x)$  for each neuron  $i \in \{f1, f2, \text{hub}, s1, s2\}$ , and thus:

$$E[T(x)] \triangleq E \begin{bmatrix} \omega_{f1}(x) \\ \vdots \\ (\omega_{f1}(x) - 0.55)^2 \\ \vdots \end{bmatrix} = \begin{bmatrix} 0.55 \\ \vdots \\ 0.025^2 \\ \vdots \end{bmatrix} \triangleq \mu, \quad (2)$$

which completes the quantification of the emergent property.

Third, we perform emergent property inference: we find a distribution over parameter configurations  $z$ , and insist that samples from this distribution produce the emergent property; in other words, they obey the constraints introduced in Equation 2. This distribution will be chosen from a family of probability distributions  $\mathcal{Q} = \{q_\theta(z) : \theta \in \Theta\}$ , defined by a deep generative model of the normalizing flow class [15, 16, 17] – neural networks which transform a simple distribution into a suitably complicated distribution (as is needed here). This deep model is represented in Figure 1E (and see Methods for more detail). Then, mathematically, we must solve the following optimization program:

$$\begin{aligned} & \underset{q_\theta \in \mathcal{Q}}{\operatorname{argmax}} H(q_\theta(z)) \\ & \text{s.t. } E_{z \sim q_\theta} [E_{x \sim p(x|z)} [T(x)]] = \mu, \end{aligned} \quad (3)$$

where  $T(x), \mu$  are defined as in Equation 3. The purpose of each element in this program is detailed in Figure 1D. Finally, we recognize that many distributions in  $\mathcal{Q}$  will respect the emergent property constraints, so we require a normative principle to select amongst them. This principle is captured in Equation 3 by the primal objective  $H$ . Here we chose Shannon entropy to model parameter distributions with minimal assumptions beyond some chosen structure [28, 29, 18, 30], but we

<sup>174</sup> emphasize that the EPI method is unaffected by this choice (the results of course will depend on  
<sup>175</sup> this choice). Stating such a problem is easy enough; finding a tractable and suitably flexible family  
<sup>176</sup> of probability distributions ( $\mathcal{Q}$ ) is hard.

<sup>177</sup> EPI optimizes the weights and biases  $\theta$  of the deep neural network (which induces the probability  
<sup>178</sup> distribution) by iteratively solving Equation 3. The optimization is complete when the sampled  
<sup>179</sup> models with parameters  $z \sim q_\theta$  produce activity consistent with the specified emergent property.  
<sup>180</sup> Such convergence is evaluated with a hypothesis test that the mean of each emergent property  
<sup>181</sup> statistic is no different than its emergent property value (see Section A.1.2). Armed with this  
<sup>182</sup> method, we now prove out the value of this technology by investigating a range of models and  
<sup>183</sup> using EPI to produce novel scientific insights.

<sup>184</sup> **3.3 Comprehensive input-responsivity in a nonlinear sensory system**

<sup>185</sup> In studies of primary visual cortex (V1), theoretical models with two populations (excitatory (E)  
<sup>186</sup> and inhibitory (I) neurons) have reproduced a host of experimentally documented phenomena. In  
<sup>187</sup> particular regimes of excitation and inhibition, these E/I models exhibit the paradoxical effect  
<sup>188</sup> [4], selective amplification [31], surround suppression [32], and sensory integrative properties [33].  
<sup>189</sup> Extending this using experimental evidence of three genetically-defined classes of inhibitory neurons  
<sup>190</sup> [34, 35], recent work [21] has investigated a four-population model – excitatory (E), parvalbumin  
<sup>191</sup> (P), somatostatin (S), and vasointestinal peptide (V) neurons – as shown in Fig. 2A. The dynamical  
<sup>192</sup> state of this model is the firing rate of each neuron-type population  $x = [x_E, x_P, x_S, x_V]^\top$ , which  
<sup>193</sup> evolves according to rectified and exponentiated dynamics:

$$\tau \frac{dx}{dt} = -x + [Wx + h]_+^n \quad (4)$$

<sup>194</sup> with effective connectivity weights  $W$  and input  $h$ . In our analysis, we set the time constant  
<sup>195</sup>  $\tau = 20\text{ms}$  and dynamics coefficient  $n = 2$ . Also, as is fairly standard, we obtain an informative  
<sup>196</sup> estimate of the effective connectivities between these neuron-types  $W$  in mice by multiplying their  
<sup>197</sup> probability of connection with their average synaptic strength [?] (see Section A.2.2). Given these  
<sup>198</sup> fixed choices of  $W$ ,  $n$ , and  $\tau$ , we studied the system’s response to input.

$$h = b + dh \quad (5)$$

<sup>199</sup> where the input  $h$  is comprised of a baseline input  $b = [b_E, b_P, b_S, b_V]$  and a differential input  
<sup>200</sup>  $dh = [dh_E, dh_P, dh_S, dh_V]$  to each neuron-type population. Throughout subsequent analyses, the  
<sup>201</sup> baseline input is  $b = [1, 1, 1, 1]$ .

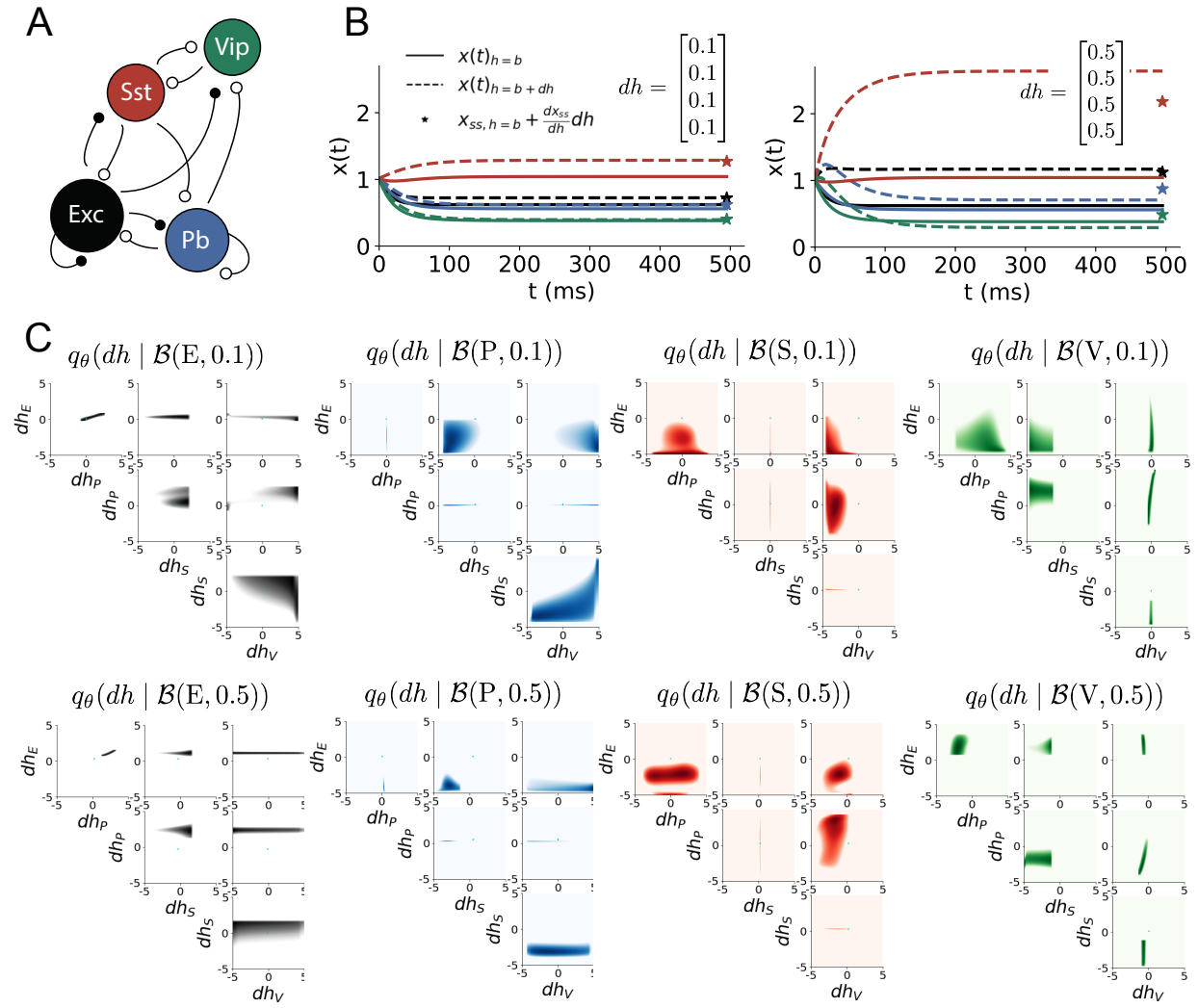


Figure 2: Exploring neuron-type responsivity in V1. A. Four-population model of primary visual cortex with excitatory (black), parvalbumin (blue), somatostatin (red), and vip (green) neurons. Some neuron-types largely do not form synaptic projections to others (excitatory and inhibitory projections filled and unfilled, respectively). B. Linear response predictions become inaccurate with greater input strength. V1 model simulations for input (solid)  $h = b$  and (dashed)  $h = b + dh$  with  $b = [1, 1, 1, 1]^\top$  and (left)  $dh = [0.1, 0.1, 0.1, 0.1]^\top$  (right)  $dh = [0.5, 0.5, 0.5, 0.5]^\top$ . Stars indicate the linear response prediction. C. EPI distributions on differential input  $dh$  conditioned on differential response  $\mathcal{B}(\alpha, y)$  (see text). The linear prediction from two standard deviations away from  $y$  (from negative to positive) is overlaid in cyan (very small, near origin).

Having established our model, we now turn to defining the emergent property. We begin with the linearized response of the system  $\frac{dx_{ss}}{dh}$  at fixed points  $x_{ss}$ . While this linearization accurately predicts differential responses  $dx_{ss} = [dx_{E,ss} \ dx_{P,ss} \ dx_{S,ss} \ dx_{V,ss}]$  for small differential inputs to each population  $dh = [0.1 \ 0.1 \ 0.1 \ 0.1]$  (Fig. 2B, left), it can be misleading in such a nonlinear model for a greater differential input strength  $dh = [0.1 \ 0.1 \ 0.1 \ 0.1]$  (Fig. 3B, right). In fact, the linearly predicted response for the V-population to  $dh = [0.5 \ 0.5 \ 0.5 \ 0.5]$  was actually in the opposite direction of the true response (Fig. 2B, right, green). This shows that currently available approaches to deriving the steady state response of this system are limited.

To get a more comprehensive picture of the input-responsivity of each neuron-type, we used EPI to learn a distribution of differential inputs  $dh$  that cause the rate of each neuron-type population  $\alpha \in \{E, P, S, V\}$  to increase by a value  $y \in 0.1, 0.5$  denoted by the emergent property

$$\mathcal{B}(\alpha, y) \leftrightarrow E \begin{bmatrix} dx_{\alpha,ss} \\ (dx_{\alpha,ss} - y)^2 \end{bmatrix} = \begin{bmatrix} y \\ 0.01^2 \end{bmatrix} \quad (6)$$

Note that we restrict the variance of the emergent property statistic  $dx_{\alpha,ss}$  by setting its second moment to a small value. In Fig. 2C, each column visualizes the inferred distribution of  $dh$  corresponding to a specific neuron-type increase, while each row corresponds to amounts of increase 0.1 and 0.5. For visualization of this four-dimensional distribution, we show the two-dimensional marginal densities. The inferred distributions suggest a slate of testable hypotheses. 1. As expected, each neuron-type's rate is sensitive to its direct input. 2. The E- and P-populations are largely unaffected by  $dh_V$ . 3. Similarly, The S-population is largely unaffected by  $dh_P$ . 4. Since EPI showed that negative  $dh_E$  results in small  $dx_{V,ss}$ , but positive  $dh_E$  elicited a larger  $dx_{V,ss}$  we predict that there is a nonmonotonic response of  $dx_{V,ss}$  with  $dh_E$ .

We evaluate these hypotheses by taking steps in individual neuron-type input  $\Delta h_\alpha$  away from the modes of the inferred distributions

$$dh^* = z^* = \underset{z}{\operatorname{argmax}} \log q_\theta(z | \mathcal{B}(\alpha, 0.1)) \quad (7)$$

Now,  $dx_{\alpha,ss}$  is the steady state response to the system with input  $h = b + dh^* + \Delta h_\alpha u_\alpha$  where  $u_\alpha$  is a unit vector in the dimension of  $\alpha$ . Our hypotheses suggested by EPI are confirmed. 1. the neuron-type responses are sensitive to their direct inputs (Fig. 3A black, 3B blue, 3C red, 3D green), 2. the E- and P-populations are not affected by  $dh_V$  (Fig. 3A green, 3B green), 3. the S-population is not affected by  $dh_P$  (Fig. 3C blue), and 4. the V-population has a nonmonotonic response to  $dh_E$  (Fig. 3D black). All of this validated insight gained beyond what the analytic linear prediction told us (Fig. 2C, cyan).

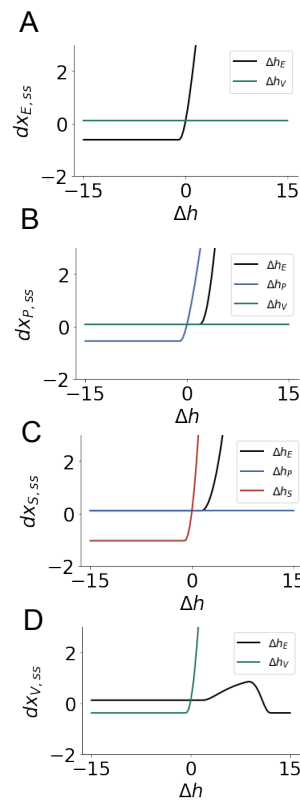


Figure 3: Confirming EPI generated hypotheses in V1. A. Differential responses by the E-population to changes in individual input  $\Delta h_\alpha u_\alpha$  away from the mode of the EPI distribution  $dh^*$ . B-D Same plots for the P-, S-, and V-populations for the inputs for which hypotheses were formulated.

231 To this point, we have shown the utility of EPI on relatively low-level emergent properties like  
 232 network syncing and differential neuron-type population responses. In the remainder of the study,  
 233 we focus on using EPI to understand models of more abstract cognitive function.

### 234 3.4 Identifying neural mechanisms of behavioral learning.

235 Identifying measurable biological changes that result in improved behavior is important for neuro-  
 236 science, since they may indicate how the learning brain adapts. In a rapid task switching exper-  
 237 iment [36], where rats were to respond right (R) or left (L) to the side of a light stimulus in the  
 238 pro (P) task, and oppositely in the anti (A) task predicated by an auditory cue (Fig. 3A), neural  
 239 recordings exhibited two population of neurons in each hemisphere of superior colliculus (SC) that  
 240 simultaneously represented both task condition and motor response: the Pro/contralateral and  
 241 Anti/ipsilateral neurons [22]. Duan et al. proposed a model of SC that, like the V1 model analyzed  
 242 in the previous section, is a four-population dynamical system. Here, the neuron-type populations  
 243 are functionally-defined as the Pro- and Anti-populations in each hemisphere (left (L) and right  
 244 (R)). The Pro- or Anti-populations receive an input determined by the cue, and then the left and  
 245 right populations receive an input based on the side of the light stimulus. Activities were bounded

from 0-1, so that a high output (1) of the Pro population in a given hemisphere corresponds to the contralateral response. An additional stipulation is that when one Pro population responds with a high-output, the opposite Pro population must respond with a low output (0). Finally, this circuit operates in the presence of gaussian noise resulting in trial-to-trial variability (see Section A.2.3). The connectivity matrix is parameterized by the geometry of the population arrangement (Fig. 3B).

Here, we used EPI to learn connectivity distributions consistent with various levels of accuracy in the rapid task switching behavioral paradigm. EPI was used to learn distributions of the SC weight matrix parameters  $z = W$  conditioned on of various levels of rapid task switching accuracy  $\mathcal{B}(p)$  for  $p \in \{50\%, 60\%, 70\%, 80\%, 90\%\}$  (see Section A.2.3). There is a decomposition for of the connectivity matrix  $W = QAQ^{-1}$ , in which the eigenvectors  $q_i$  are the same for all  $W$  (Fig. 3C). These consistent eigenvectors have intuitive roles in processing for this task, and are accordingly named the *all* - all neurons co-fluctuate, *side* - one side dominates the other, *task* - the Pro or Anti populations dominate the other, and *diag* - Pro- and Anti-populations of opposite hemispheres dominate the opposite pair. The corresponding eigenvalues (e.g.  $a_{\text{task}}$ , which change according to  $W$ ) indicate the degree to which activity along that mode is increased or decreased by  $W$ .

For greater task accuracies, the task mode eigenvalue increases, indicating the criticality of supporting the task representation in the connectivity of  $W$ , (Fig. 4D, purple). Stepping from random chance (50%) networks to marginally task-performing (60%) networks, there is a marked decrease of the side mode eigenvalues (Fig. 3D, orange). Such side mode suppression remains in the models achieving greater accuracy, revealing its importance towards task performance. There were no interesting trends with learning in the all or diag mode. Significantly, we can conclude from our methodology optimized to find all connectivities consistent with a level of accuracy, that side mode suppression in  $W$  allows rapid task switching, and that greater task-mode representations in  $W$  increase accuracy. These hypotheses are proved out in the model (Fig. 3E). Thus, our EPI-enabled analyses produce novel, experimentally testable predictions that effective connectivity between these populations changes throughout learning in a way that increases its task mode and decreases its side mode eigenvalues.

### 3.5 Characterizing the sources of bias in RNN computation

So far, each biologically realistic model we have studied was designed from fundamental biophysical principles, genetically- or functionally-defined neuron types. At a more abstract level of modeling,

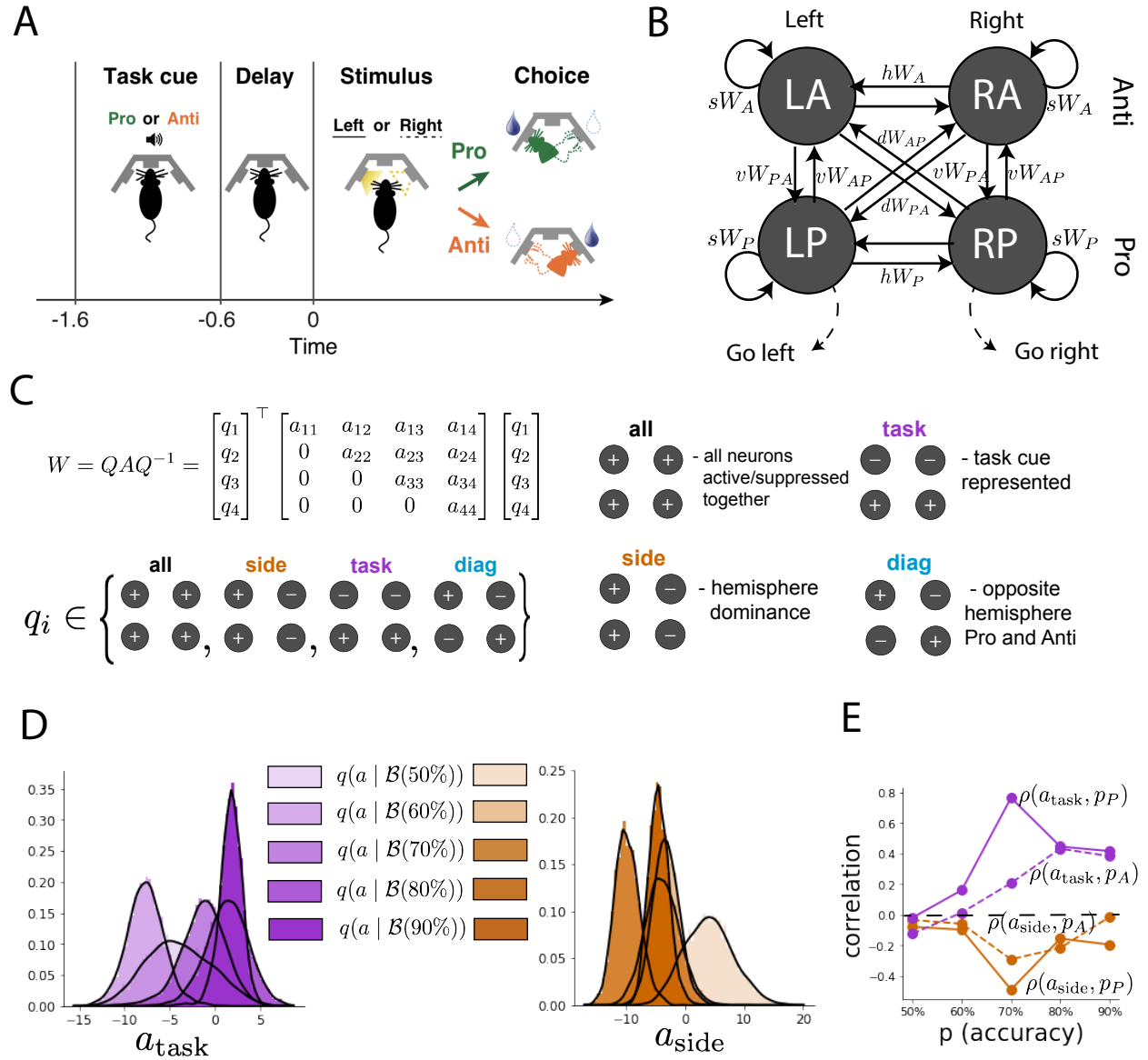


Figure 4: EPI reveals changes in SC [22] connectivity that result in greater task accuracy. A. Rapid task switching behavioral paradigm. In the Pro (Anti) condition indicated by an auditory cue, rats respond by poking into a side port to the same (opposite) side as the light stimulus that is provided after a delay to receive a reward. B. Model of superior colliculus (SC). Neurons: LP - left pro, RP - right pro, LA - left anti, RA - right anti. Parameters:  $sW$  - self,  $hW$  - horizontal,  $vW$  - vertical,  $dW$  - diagonal weights. C. The Schur decomposition of the weight matrix  $W = QAQ^{-1}$  is a unique decomposition with orthogonal  $Q$  and upper triangular  $A$ . The invariant Schur eigenmodes (symmetry of  $W$ ) are labeled by their hypothesized role in computation:  $q_{\text{all}}$ ,  $q_{\text{task}}$ ,  $q_{\text{side}}$ , and  $q_{\text{diag}}$ . The values of  $A$  are what change for different realizations of  $W$ . D. The marginal EPI distributions of the Schur eigenvalues at each level of task accuracy. E. The correlation of Schur eigenvalue with task performance in each learned EPI distribution.

277 recurrent neural networks (RNNs) are high-dimensional models of computation, which have become  
 278 increasingly popular in neuroscience research [37]. Typically, RNNs are trained to do a task from a  
 279 systems neuroscience experiment, and then the unit activations of the trained RNN are compared  
 280 to recorded neural activity. A monumental challenge for this line of work is to link findings at  
 281 this level of abstraction with interpretable biophysical mechanisms in the brain. Here we leverage  
 282 recent theoretical work to run EPI on interpretable parameterizations of RNN connectivity solving  
 283 a toy problem.

284 Importantly, recent work establishes such a link between RNN connectivity weights and the re-  
 285 sulting dynamical responses of the network using dynamic mean field theory (DMFT) for neural  
 286 networks [3]. Specifically, DMFT describes the properties of activity in infinite-size neural networks  
 287 given a distribution on the connectivity weights. This theory has been extended from random neural  
 288 networks to low rank RNNs, which have low-dimensional parameterizations of RNN connectivity  
 289 via the pairwise correlations of the low-rank vectors (i.e. the low-rank “geometry”) [23]. For  
 290 example, the connectivity of a rank-1 RNN  $J$  is the sum of a random component with strength  
 291 determined by  $g$  and a structured component determined by the outer product of vectors  $m$  and  $n$ :

$$J = g\chi + \frac{1}{N}mn^\top \quad (8)$$

292 where the activity  $x$  evolves as

$$\frac{\partial x}{\partial t} = -x(t) + J\phi(x(t)) + I(t) \quad (9)$$

293  $I(t)$  is some input,  $\phi$  is the tanh nonlinearity, and  $\chi_{ij} \sim \mathcal{N}(0, \frac{1}{N})$ . The entries of  $m$  and  $n$  are  
 294 drawn from gaussian distributions  $m_i \sim \mathcal{N}(M_m, 1)$  and  $n_i \sim \mathcal{N}(M_n, 1)$ , whose parameters  $M_m$  and  
 295  $M_n$  determine their degree of correlation.

296 Mastrogiuseppe et al. are able to design low-rank connectivities via the pairwise correlations of such  
 297 low-rank vectors that solve tasks from behavioral neuroscience. An important detail is that a non-  
 298 linear system of equations solver must be used to obtain the task-relevant variables of interest from  
 299 the derived consistency equations (see Section A.2.4). However, we can consider the DMFT equa-  
 300 tion solver as a black box that takes in a low-rank parameterization  $z$  (e.g.  $z = [g \ M_m \ M_n]$ ) and  
 301 outputs task-relevant response variables (e.g. average network activity  $\mu$ , the temporal variability  
 302 in the network  $\Delta_T$ , or network activity along a given dimension  $\kappa$ ). Furthermore, we recognize that  
 303 the solution produced by the solver is differentiable with respect to the input parameters. Thus, we  
 304 are able to combine this DMFT with EPI to learn distributions on such connectivity parameters

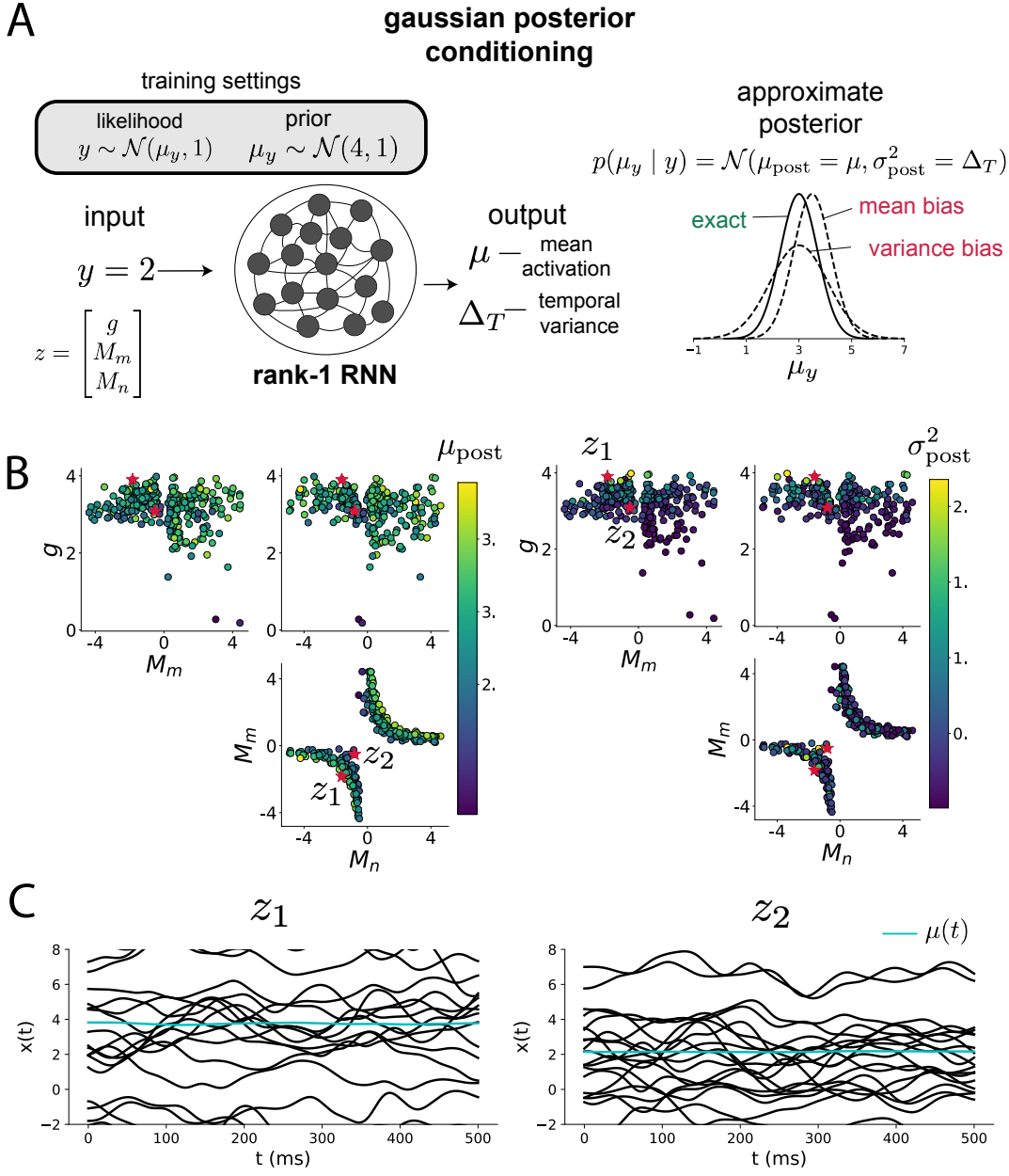


Figure 5: Sources of bias in RNN computation. A. (left) A rank-1 RNN running approximate Bayesian inference on  $\mu_y$  assuming a gaussian likelihood variance of 1 and a prior of  $\mathcal{N}(4, 1)$ . (center) The rank-1 RNN represents the computed gaussian posterior mean  $\mu_{\text{post}}$  and variance  $\sigma_{\text{post}}^2$  in its mean activity  $\mu$  and its temporal variance  $\Delta_T$ . (right) Bias in this computation can come from over- or under-estimating the posterior mean or variance. B. Distribution of rank-1 RNNs executing approximate Bayesian inference. Samples are colored by (left) posterior mean  $\mu_{\text{post}} = \mu$  and (right) posterior variance  $\sigma_{\text{post}}^2 = \Delta_T$ . C. Finite size realizations agree with the DMFT theory.

305 of RNNs that execute neuroscientific tasks via an emergent property defined on the task-relevant  
 306 responses produced by DMFT.

307 For our toy problem, we consider the emergent property of gaussian posterior conditioning. Specif-  
 308 ically, we ask the RNN to calculate the parameters of a gaussian posterior distribution on the mean  
 309 of a gaussian likelihood  $\mu_y$  given a single observation of  $y$  and a gaussian prior  $p(\mu_y) = \mathcal{N}(4, 1)$   
 310 (Fig. 5A). Assuming the variance of the gaussian likelihood is 1, the true posterior for an input of  
 311  $y = 2$  is  $p(\mu_y | y) = \mathcal{N}(3, 0.5)$ . We used EPI to learn distributions of RNNs producing the correct  
 312 posterior mean and variance in their mean activity  $\mu = \mu_{\text{post}}$  and temporal variance  $\Delta_T = \sigma_{\text{post}}^2$   
 313 given an input of  $y = 2$ . (see Section A.2.4) (Fig. 5B).

314 When specifying the emergent property of gaussian posterior conditioning, we allowed a substan-  
 315 tial amount of variability in the second moment constraints of the network mean  $\mu$  and temporal  
 316 variance  $\Delta_T$ . This resulted in a distribution of rank-1 RNN parameterizations having a wide vari-  
 317 ety biases in the resulting  $\mu_{\text{post}}$  and  $\sigma_{\text{post}}^2$  (under- or over-estimations of the posterior means and  
 318 variances). We can examine the nature of the biases in this toy computation by visualizing the  
 319 produced posterior means (Fig. 5B, left) and variances (Fig. 5B, right) in the inferred distribution.  
 320 The inferred distribution has roughly symmetric in the  $M_m$ - $M_n$  plane, suggesting there is a degen-  
 321 eracy in the product of  $M_m$  and  $M_n$  (Fig. 5B). The product of  $M_m$  and  $M_n$  almost completely  
 322 determines the posterior mean (Fig. 5B, left), and the random strength  $g$  is the most influential  
 323 variable on the temporal variance (Fig. 5B, right). Neither of these observations were obvious from  
 324 the consistency equations afforded by DMFT (see Section A.2.4).

325 When working with DMFT, it's important to check that finite-size realizations of these infinite-  
 326 size networks match the theoretical predictions. We check 2,000-neuron realizations of drawn  
 327 parameters  $z_1$  and  $z_2$  from the inferred distribution.  $z_1$  has relatively high  $g$  and high  $M_m M_n$ ,  
 328 whereas  $z_2$  has relatively low  $g$  and low  $M_m M_n$ . Confirming our intuition,  $z_1$  overestimates the  
 329 posterior mean, since mean activity  $\mu(t) > 3$  (Fig. 5C, left cyan). In turn,  $z_2$  underestimates the  
 330 posterior mean, since  $\mu(t) < 3$  (Fig. 5C, right cyan). Finally,  $z_1$  results in evidently greater temporal  
 331 variance than  $z_2$ . This novel procedure of doing inference in interpretable parameterizations of  
 332 RNNs conditioned on task execution is straightforwardly generalizable to other tasks like noisy  
 333 integration and context-dependent decision making (Fig. S1).

## <sup>334</sup> 4 Discussion

### <sup>335</sup> 4.1 EPI is a general tool for theoretical neuroscience.

<sup>336</sup> Models of biological systems often have complex nonlinear differential equations, making traditional  
<sup>337</sup> statistical inference intractable. In contrast, EPI is capable of learning distributions of parameters  
<sup>338</sup> in such models producing measurable signatures of computation. We have demonstrated its utility  
<sup>339</sup> on biological models (STG), intermediate-level models of interacting genetically- and functionally-  
<sup>340</sup> defined neuron-types (V1, SC), and the most abstract of models (RNNs). We are able to condi-  
<sup>341</sup> tion both deterministic and stochastic models on low-level emergent properties like firing rates of  
<sup>342</sup> membrane potentials, as well as high-level cognitive function like approximate Bayesian inference.  
<sup>343</sup> Technically, EPI is tractable when the emergent property statistics are continuously differentiable  
<sup>344</sup> with respect to the model parameters, which is very often the case; this emphasizes the general  
<sup>345</sup> utility of EPI.

<sup>346</sup> In this study, we have focused on applying EPI to low dimensional parameter spaces of models  
<sup>347</sup> with low dimensional dynamical state. These choices were made to present the reader with a series  
<sup>348</sup> of interpretable conclusions, which is more challenging in high dimensional spaces. In fact, EPI  
<sup>349</sup> should scale reasonably to high dimensional parameter spaces, as the underlying technology has  
<sup>350</sup> produced state-of-the-art performance on high-dimensional tasks such as texture generation [18].  
<sup>351</sup> Of course, increasing the dimensionality of the dynamical state of the model makes optimization  
<sup>352</sup> more expensive, and there is a practical limit there as with any machine learning approach. For  
<sup>353</sup> systems with high dimensional state, we recommend using theoretical approaches (e.g. [23]) to  
<sup>354</sup> reason about reduced parameterizations of such high-dimensional systems.

<sup>355</sup> There are additional technical considerations when assessing the suitability of EPI for a particu-  
<sup>356</sup> lar modeling question. First and foremost, as in any optimization problem, the defined emergent  
<sup>357</sup> property should always be appropriately conditioned (constraints should not have wildly different  
<sup>358</sup> units). Furthermore, if the program is underconstrained (not enough constraints), the distribution  
<sup>359</sup> grows (in entropy) unstably unless mapped to a finite support. If overconstrained, there is no pa-  
<sup>360</sup> rameter set producing the emergent property, and EPI optimization will fail (appropriately). Next,  
<sup>361</sup> one should consider the computational cost of the gradient calculations. In the best circumstance,  
<sup>362</sup> there is a simple, closed form expression (e.g. Section A.1.1) for the emergent property statistic  
<sup>363</sup> given the model parameters. On the other end of the spectrum, many forward simulation iterations  
<sup>364</sup> may be required before a high quality measurement of the emergent property statistic is available

365 (e.g. Section A.2.1). In such cases, optimization will be expensive.

366 **4.2 Novel hypotheses from EPI**

367 Machine learning has played an effective, multifaceted role in neuroscientific progress. Primarily,  
368 it has revealed structure in large-scale neural datasets [39, 40, 41, 42, 43, 44] (see review, [14]).  
369 Secondarily, trained algorithms of varying degrees of biological relevance are beginning to be viewed  
370 as fully-observable computational systems comparable to the brain [45, 46]. Theorists can use deep  
371 learning for probabilistic inference to understand their models and their behavior.

372 For example, consider the fact that we do not yet understand just a four-dimensional, deterministic  
373 model of V1 [21]. This should not be surprising, since analytic approaches to studying nonlinear  
374 dynamical systems become increasingly complicated when stepping from two-dimensional to three-  
375 or four-dimensional systems in the absence of restrictive simplifying assumptions [47]. We promote  
376 the recognition of analytic difficulty, and alternatively the use of EPI to gain the desired model  
377 insights. In Section 3.3, we showed that EPI was far more informative about neuron-type input  
378 responsivity than the predictions afforded through analysis. By flexibly conditioning this V1 model  
379 on different emergent properties, we performed an exploratory analysis of a *model* rather than a  
380 dataset, which generated and proved out a set of testable predictions.

381 Exploratory analyses can be directed. For example, when interested in model changes during learn-  
382 ing, one can use EPI to condition on various levels of an emergent property statistic indicative of  
383 performance like task accuracy in a behavioral paradigm (see Section 3.4). This analysis iden-  
384 tified experimentally testable predictions (proved out *in-silico*) of changes in connectivity in SC  
385 throughout learning of a rapid task switching behavior. Precisely, we predict an initial reduction  
386 in side mode eigenvalue, and a steady increase in task mode eigenvalue in the effective connectivity  
387 matrices of learning rats.

388 In our final analysis, we present a novel procedure for doing statistical inference on interpretable  
389 parameterizations of RNNs executing tasks from behavioral neuroscience. This methodology relies  
390 on recently extended theory of responses in random neural networks with minimal structure [23].  
391 With this methodology, we can finally open the probabilistic model selection toolkit reasoning  
392 about the connectivity of RNNs solving tasks.

## 393 References

- 394 [1] Larry F Abbott. Theoretical neuroscience rising. *Neuron*, 60(3):489–495, 2008.
- 395 [2] John J Hopfield. Neurons with graded response have collective computational properties like  
396 those of two-state neurons. *Proceedings of the national academy of sciences*, 81(10):3088–3092,  
397 1984.
- 398 [3] Haim Sompolinsky, Andrea Crisanti, and Hans-Jurgen Sommers. Chaos in random neural  
399 networks. *Physical review letters*, 61(3):259, 1988.
- 400 [4] Misha V Tsodyks, William E Skaggs, Terrence J Sejnowski, and Bruce L McNaughton. Para-  
401 doxical effects of external modulation of inhibitory interneurons. *Journal of neuroscience*,  
402 17(11):4382–4388, 1997.
- 403 [5] Diederik P Kingma and Max Welling. Auto-encoding variational bayes. *International Confer-  
404 ence on Learning Representations*, 2014.
- 405 [6] Danilo Jimenez Rezende, Shakir Mohamed, and Daan Wierstra. Stochastic backpropagation  
406 and variational inference in deep latent gaussian models. *International Conference on Machine  
407 Learning*, 2014.
- 408 [7] Yuanjun Gao, Evan W Archer, Liam Paninski, and John P Cunningham. Linear dynamical  
409 neural population models through nonlinear embeddings. In *Advances in neural information  
410 processing systems*, pages 163–171, 2016.
- 411 [8] Yuan Zhao and Il Memming Park. Recursive variational bayesian dual estimation for nonlinear  
412 dynamics and non-gaussian observations. *stat*, 1050:27, 2017.
- 413 [9] Gabriel Barello, Adam Charles, and Jonathan Pillow. Sparse-coding variational auto-encoders.  
414 *bioRxiv*, page 399246, 2018.
- 415 [10] Chethan Pandarinath, Daniel J O’Shea, Jasmine Collins, Rafal Jozefowicz, Sergey D Stavisky,  
416 Jonathan C Kao, Eric M Trautmann, Matthew T Kaufman, Stephen I Ryu, Leigh R Hochberg,  
417 et al. Inferring single-trial neural population dynamics using sequential auto-encoders. *Nature  
418 methods*, page 1, 2018.
- 419 [11] Alexander B Wiltschko, Matthew J Johnson, Giuliano Iurilli, Ralph E Peterson, Jesse M  
420 Katon, Stan L Pashkovski, Victoria E Abraira, Ryan P Adams, and Sandeep Robert Datta.  
421 Mapping sub-second structure in mouse behavior. *Neuron*, 88(6):1121–1135, 2015.

- [422] [12] Matthew J Johnson, David K Duvenaud, Alex Wiltschko, Ryan P Adams, and Sandeep R Datta. Composing graphical models with neural networks for structured representations and fast inference. In *Advances in neural information processing systems*, pages 2946–2954, 2016.
- [425] [13] Eleanor Batty, Matthew Whiteway, Shreya Saxena, Dan Biderman, Taiga Abe, Simon Musall, Winthrop Gillis, Jeffrey Markowitz, Anne Churchland, John Cunningham, et al. Behavenet: nonlinear embedding and bayesian neural decoding of behavioral videos. *Advances in Neural Information Processing Systems*, 2019.
- [429] [14] Liam Paninski and John P Cunningham. Neural data science: accelerating the experiment-analysis-theory cycle in large-scale neuroscience. *Current opinion in neurobiology*, 50:232–241, 2018.
- [432] [15] Danilo Jimenez Rezende and Shakir Mohamed. Variational inference with normalizing flows. *International Conference on Machine Learning*, 2015.
- [434] [16] Laurent Dinh, Jascha Sohl-Dickstein, and Samy Bengio. Density estimation using real nvp. *arXiv preprint arXiv:1605.08803*, 2016.
- [436] [17] George Papamakarios, Theo Pavlakou, and Iain Murray. Masked autoregressive flow for density estimation. In *Advances in Neural Information Processing Systems*, pages 2338–2347, 2017.
- [438] [18] Gabriel Loaiza-Ganem, Yuanjun Gao, and John P Cunningham. Maximum entropy flow networks. *International Conference on Learning Representations*, 2017.
- [440] [19] Dustin Tran, Rajesh Ranganath, and David Blei. Hierarchical implicit models and likelihood-free variational inference. In *Advances in Neural Information Processing Systems*, pages 5523–5533, 2017.
- [443] [20] Gabrielle J Gutierrez, Timothy O’Leary, and Eve Marder. Multiple mechanisms switch an electrically coupled, synaptically inhibited neuron between competing rhythmic oscillators. *Neuron*, 77(5):845–858, 2013.
- [446] [21] Ashok Litwin-Kumar, Robert Rosenbaum, and Brent Doiron. Inhibitory stabilization and visual coding in cortical circuits with multiple interneuron subtypes. *Journal of neurophysiology*, 115(3):1399–1409, 2016.

- 449 [22] Chunyu A Duan, Marino Pagan, Alex T Piet, Charles D Kopec, Athena Akrami, Alexander J  
450 Riordan, Jeffrey C Erlich, and Carlos D Brody. Collicular circuits for flexible sensorimotor  
451 routing. *bioRxiv*, page 245613, 2018.
- 452 [23] Francesca Mastrogiovanni and Srdjan Ostojic. Linking connectivity, dynamics, and computa-  
453 tions in low-rank recurrent neural networks. *Neuron*, 99(3):609–623, 2018.
- 454 [24] Sean R Bittner, Agostina Palmigiano, Kenneth D Miller, and John P Cunningham. Degener-  
455 ate solution networks for theoretical neuroscience. *Computational and Systems Neuroscience  
456 Meeting (COSYNE), Lisbon, Portugal*, 2019.
- 457 [25] Sean R Bittner, Alex T Piet, Chunyu A Duan, Agostina Palmigiano, Kenneth D Miller,  
458 Carlos D Brody, and John P Cunningham. Examining models in theoretical neuroscience with  
459 degenerate solution networks. *Bernstein Conference*, 2019.
- 460 [26] Jan-Matthis Lueckmann, Pedro Goncalves, Chaitanya Chintaluri, William F Podlaski, Gia-  
461 como Bassetto, Tim P Vogels, and Jakob H Macke. Amortised inference for mechanistic models  
462 of neural dynamics. In *Computational and Systems Neuroscience Meeting (COSYNE), Lisbon,  
463 Portugal*, 2019.
- 464 [27] Eve Marder and Vatsala Thirumalai. Cellular, synaptic and network effects of neuromodula-  
465 tion. *Neural Networks*, 15(4-6):479–493, 2002.
- 466 [28] Edwin T Jaynes. Information theory and statistical mechanics. *Physical review*, 106(4):620,  
467 1957.
- 468 [29] Gamaleldin F Elsayed and John P Cunningham. Structure in neural population recordings:  
469 an expected byproduct of simpler phenomena? *Nature neuroscience*, 20(9):1310, 2017.
- 470 [30] Cristina Savin and Gašper Tkačik. Maximum entropy models as a tool for building precise  
471 neural controls. *Current opinion in neurobiology*, 46:120–126, 2017.
- 472 [31] Brendan K Murphy and Kenneth D Miller. Balanced amplification: a new mechanism of  
473 selective amplification of neural activity patterns. *Neuron*, 61(4):635–648, 2009.
- 474 [32] Hirofumi Ozeki, Ian M Finn, Evan S Schaffer, Kenneth D Miller, and David Ferster. Inhibitory  
475 stabilization of the cortical network underlies visual surround suppression. *Neuron*, 62(4):578–  
476 592, 2009.

- 477 [33] Daniel B Rubin, Stephen D Van Hooser, and Kenneth D Miller. The stabilized supralinear  
478 network: a unifying circuit motif underlying multi-input integration in sensory cortex. *Neuron*,  
479 85(2):402–417, 2015.
- 480 [34] Henry Markram, Maria Toledo-Rodriguez, Yun Wang, Anirudh Gupta, Gilad Silberberg, and  
481 Caizhi Wu. Interneurons of the neocortical inhibitory system. *Nature reviews neuroscience*,  
482 5(10):793, 2004.
- 483 [35] Bernardo Rudy, Gordon Fishell, SooHyun Lee, and Jens Hjerling-Leffler. Three groups of  
484 interneurons account for nearly 100% of neocortical gabaergic neurons. *Developmental neuro-*  
485 *biology*, 71(1):45–61, 2011.
- 486 [36] Chunyu A Duan, Jeffrey C Erlich, and Carlos D Brody. Requirement of prefrontal and midbrain  
487 regions for rapid executive control of behavior in the rat. *Neuron*, 86(6):1491–1503, 2015.
- 488 [37] Omri Barak. Recurrent neural networks as versatile tools of neuroscience research. *Current*  
489 *opinion in neurobiology*, 46:1–6, 2017.
- 490 [38] Laurence Aitchison and Máté Lengyel. With or without you: predictive coding and bayesian  
491 inference in the brain. *Current opinion in neurobiology*, 46:219–227, 2017.
- 492 [39] Robert E Kass and Valérie Ventura. A spike-train probability model. *Neural computation*,  
493 13(8):1713–1720, 2001.
- 494 [40] Emery N Brown, Loren M Frank, Dengda Tang, Michael C Quirk, and Matthew A Wilson.  
495 A statistical paradigm for neural spike train decoding applied to position prediction from  
496 ensemble firing patterns of rat hippocampal place cells. *Journal of Neuroscience*, 18(18):7411–  
497 7425, 1998.
- 498 [41] Liam Paninski. Maximum likelihood estimation of cascade point-process neural encoding  
499 models. *Network: Computation in Neural Systems*, 15(4):243–262, 2004.
- 500 [42] M Yu Byron, John P Cunningham, Gopal Santhanam, Stephen I Ryu, Krishna V Shenoy, and  
501 Maneesh Sahani. Gaussian-process factor analysis for low-dimensional single-trial analysis  
502 of neural population activity. In *Advances in neural information processing systems*, pages  
503 1881–1888, 2009.

- 504 [43] Kenneth W Latimer, Jacob L Yates, Miriam LR Meister, Alexander C Huk, and Jonathan W  
 505 Pillow. Single-trial spike trains in parietal cortex reveal discrete steps during decision-making.  
 506 *Science*, 349(6244):184–187, 2015.
- 507 [44] Lea Duncker, Gergo Bohner, Julien Boussard, and Maneesh Sahani. Learning interpretable  
 508 continuous-time models of latent stochastic dynamical systems. *Proceedings of the 36th Inter-*  
 509 *national Conference on Machine Learning*, 2019.
- 510 [45] David Sussillo and Omri Barak. Opening the black box: low-dimensional dynamics in high-  
 511 dimensional recurrent neural networks. *Neural computation*, 25(3):626–649, 2013.
- 512 [46] Blake A Richards and et al. A deep learning framework for neuroscience. *Nature Neuroscience*,  
 513 2019.
- 514 [47] Steven H Strogatz. Nonlinear dynamics and chaos: with applications to physics. *Biology,*  
 515 *Chemistry, and Engineering (Studies in Nonlinearity)*, Perseus, Cambridge, UK, 1994.
- 516 [48] Rajesh Ranganath, Sean Gerrish, and David Blei. Black box variational inference. In *Artificial*  
 517 *Intelligence and Statistics*, pages 814–822, 2014.
- 518 [49] Martin J Wainwright, Michael I Jordan, et al. Graphical models, exponential families, and  
 519 variational inference. *Foundations and Trends® in Machine Learning*, 1(1–2):1–305, 2008.
- 520 [50] Laurent Dinh, Jascha Sohl-Dickstein, and Samy Bengio. Density estimation using real nvp.  
 521 *Proceedings of the 5th International Conference on Learning Representations*, 2017.
- 522 [51] David M Blei, Alp Kucukelbir, and Jon D McAuliffe. Variational inference: A review for  
 523 statisticians. *Journal of the American Statistical Association*, 112(518):859–877, 2017.
- 524 [52] Carsten K Pfeffer, Mingshan Xue, Miao He, Z Josh Huang, and Massimo Scanziani. Inhi-  
 525 bition of inhibition in visual cortex: the logic of connections between molecularly distinct  
 526 interneurons. *Nature neuroscience*, 16(8):1068, 2013.

527 **A Methods**

528 **A.1 Emergent property inference (EPI)**

529 Emergent property inference (EPI) learns distributions of theoretical model parameters that pro-  
 530 duce emergent properties of interest. EPI combines ideas from likelihood-free variational inference

[19] and maximum entropy flow networks [18]. A maximum entropy flow network is used as a deep probability distribution for the parameters, while these samples often parameterize a differentiable model simulator, which may lack a tractable likelihood function.

Consider model parameterization  $z$  and data  $x$  generated from some theoretical model simulator represented as  $p(x | z)$ , which may be deterministic or stochastic. Theoretical models usually have known sampling procedures for simulating activity given a circuit parameterization, yet often lack an explicit likelihood function due to the nonlinearities and dynamics. With EPI, a distribution on parameters  $z$  is learned, that yields an emergent property of interest  $\mathcal{B}$ ,

$$\mathcal{B} \leftrightarrow E_{z \sim q_\theta} [E_{x \sim p(x|z)} [T(x)]] = \mu \quad (10)$$

by making an approximation  $q_\theta(z)$  to  $p(z | \mathcal{B})$  (see Section A.1.5). So, over the DSN distribution  $q_\theta(z)$  of model  $p(x | z)$  for behavior  $\mathcal{B}$ , the emergent properties  $T(x)$  are constrained in expectation to  $\mu$ .

In deep probability distributions, a simple random variable  $w \sim p_0$  is mapped deterministically via a function  $f_\theta$  parameterized by a neural network to the support of the distribution of interest where  $z = f_\theta(w) = f_l(\dots f_1(w))$ . Given a theoretical model  $p(x | z)$  and some behavior of interest  $\mathcal{B}$ , the deep probability distributions are trained by optimizing the neural network parameters  $\theta$  to find a good approximation  $q_\theta^*$  within the deep variational family  $Q$  to  $p(z | \mathcal{B})$ .

In most settings (especially those relevant to theoretical neuroscience) the likelihood of the behavior with respect to the model parameters  $p(T(x) | z)$  is unknown or intractable, requiring an alternative to stochastic gradient variational Bayes [5] or black box variational inference[48]. These types of methods called likelihood-free variational inference (LFVI, [19]) skate around the intractable likelihood function in situations where there is a differentiable simulator. Akin to LFVI, DSNs are optimized with the following objective for a given theoretical model, emergent property statistics  $T(x)$ , and emergent property constraints  $\mu$ :

$$\begin{aligned} q_\theta^*(z) &= \underset{q_\theta \in Q}{\operatorname{argmax}} H(q_\theta(z)) \\ \text{s.t. } E_{z \sim q_\theta} [E_{x \sim p(x|z)} [T(x)]] &= \mu \end{aligned} \quad (11)$$

Optimizing this objective is a technological accomplishment in its own right, the details of which we elaborate in Section A.1.2. Before going through those details, we ground this optimization in a toy example.

557 **A.1.1 Example: 2D LDS**

558 To gain intuition for EPI, consider two-dimensional linear dynamical systems,  $\tau \dot{x} = Ax$  with

$$A = \begin{bmatrix} a_1 & a_2 \\ a_3 & a_4 \end{bmatrix}$$

559 that produce a band of oscillations. To do EPI with the dynamics matrix elements as the free  
 560 parameters  $z = [a_1, a_2, a_3, a_4]$ , and fixing  $\tau = 1$ , such that the posterior yields a band of oscillations,  
 561 the emergent property statistics  $T(x)$  are chosen to contain the first- and second-moments of the  
 562 oscillatory frequency  $\Omega$  and the growth/decay factor  $d$  of the oscillating system. To learn the  
 563 distribution of real entries of  $A$  that yield a distribution of  $d$  with mean zero with variance  $0.25^2$ ,  
 564 and oscillation frequency  $\Omega$  with mean 1 Hz with variance  $(0.1\text{Hz})^2$ , then we would select the real  
 565 part of the complex conjugate eigenvalues  $\text{real}(\lambda_1) = d$  (via an arbitrary choice of eigenvalue of the  
 566 dynamics matrix  $\lambda_1$ ) and the positive imaginary component of one of the eigenvalues  $\text{imag}(\lambda_1) =$   
 567  $2\pi\Omega$  as the emergent property statistics. Those emergent property statistics are then constrained  
 568 to

$$\mu = E \begin{bmatrix} \text{real}(\lambda_1) \\ \text{imag}(\lambda_1) \\ (\text{real}(\lambda_1) - 0)^2 \\ (\text{imag}(\lambda_1) - 2\pi\Omega)^2 \end{bmatrix} = \begin{bmatrix} 0.0 \\ 2\pi\Omega \\ 0.25^2 \\ (2\pi 0.1)^2 \end{bmatrix} \quad (12)$$

569 where  $\Omega = 1\text{Hz}$ . Unlike the models we study in the paper which calculate  $E_{x \sim p(x|z)} [T(x)]$  via  
 570 forward simulation, we have a closed form for the eigenvalues of the dynamics matrix.  $\lambda$  can be  
 571 calculated using the quadratic formula:

$$\lambda = \frac{\left(\frac{a_1+a_4}{\tau}\right) \pm \sqrt{\left(\frac{a_1+a_4}{\tau}\right)^2 + 4\left(\frac{a_2a_3-a_1a_4}{\tau}\right)}}{2} \quad (13)$$

572 where  $\lambda_1$  is the eigenvalue of  $\frac{1}{\tau}A$  with greatest real part. Even though  $E_{x \sim p(x|z)} [T(x)]$  is calculable  
 573 directly via a closed form function and does not require simulation, we cannot derive the distribution  
 574  $q_\theta^*$  directly. This is due to the formally hard problem of the backward mapping: finding the natural  
 575 parameters  $\eta$  from the mean parameters  $\mu$  of an exponential family distribution [49]. Instead, we  
 576 can use EPI to learn the linear system parameters producing such a band of oscillations (Fig. S2B).

577 Even this relatively simple system has nontrivial (though intuitively sensible) structure in the  
 578 parameter distribution. To validate our method (further than that of the underlying technology  
 579 on a ground truth solution [18]) we can analytically derive the contours of the probability density

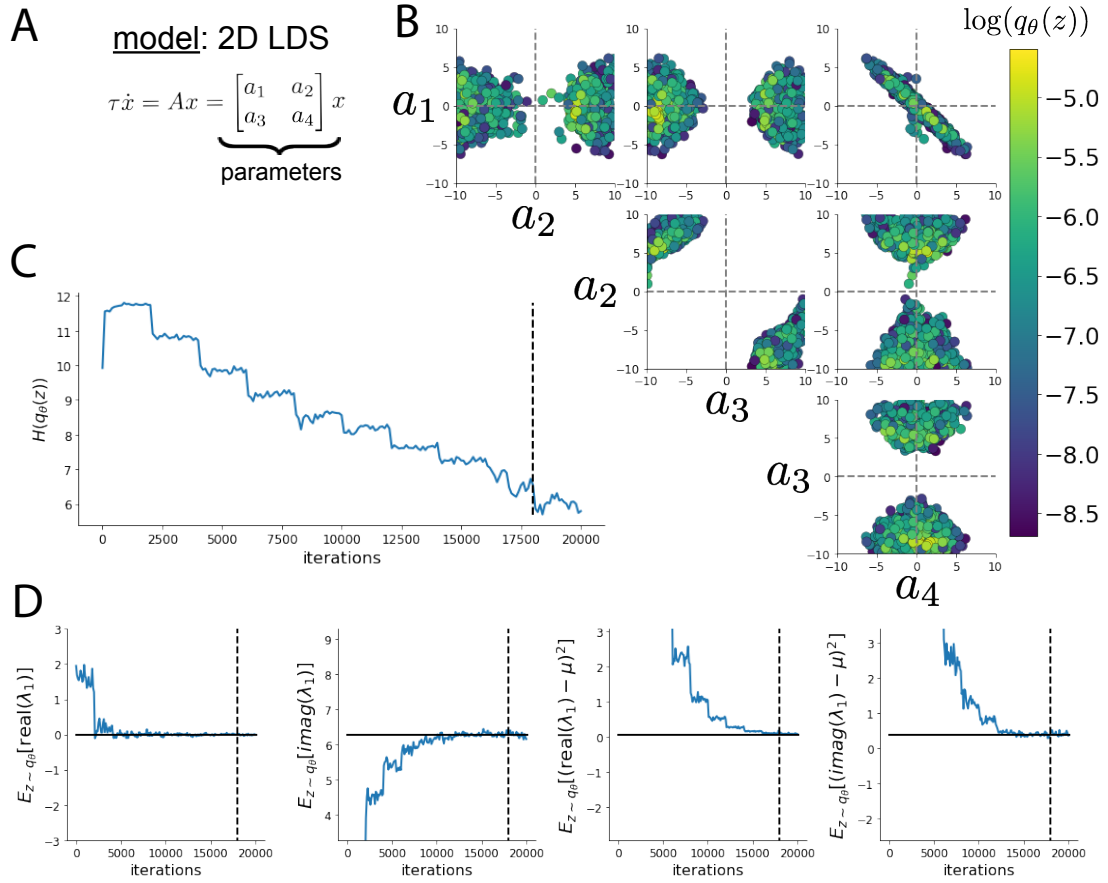


Fig. S2: A. Two-dimensional linear dynamical system model, where real entries of the dynamics matrix  $A$  are the parameters. B. The DSN distribution for a 2D LDS with  $\tau = 1$  that produces an average of 1Hz oscillations with some small amount of variance. C. Entropy throughout the optimization. At the beginning of each augmented Lagrangian epoch (5,000 iterations), the entropy dips due to the shifted optimization manifold where emergent property constraint satisfaction is increasingly weighted. D. Emergent property moments throughout optimization. At the beginning of each augmented Lagrangian epoch, the emergent property moments move closer to their constraints.

580 from the emergent property statistics and values (Fig. S3). In the  $a_1 - a_4$  plane, is a black line  
 581 at  $\text{real}(\lambda_1) = \frac{a_1 + a_4}{2} = 0$ , a dotted black line at the standard deviation  $\text{real}(\lambda_1) = \frac{a_1 + a_4}{2} \pm 1$ , and a  
 582 grey line at twice the standard deviation  $\text{real}(\lambda_1) = \frac{a_1 + a_4}{2} \pm 2$  (Fig. S3A). Here the lines denote the  
 583 set of solutions at fixed behaviors, which overlay the posterior obtained through EPI. The learned  
 584 DSN distribution precisely reflects the desired statistical constraints and model degeneracy in the  
 585 sum of  $a_1$  and  $a_4$ . Intuitively, the parameters equivalent with respect to emergent property statistic  
 586  $\text{real}(\lambda_1)$  have similar log densities.

587 To explain the structure in the bimodality of the DSN posterior, we can look at the imaginary  
 588 component of  $\lambda_1$ . When  $\text{real}(\lambda_1) = \frac{a_1 + a_4}{2} = 0$ , we have

$$\text{imag}(\lambda_1) = \begin{cases} \sqrt{\frac{a_1 a_4 - a_2 a_3}{\tau}}, & \text{if } a_1 a_4 < a_2 a_3 \\ 0 & \text{otherwise} \end{cases} \quad (14)$$

589 When  $\tau = 1$  and  $a_1 a_4 > a_2 a_3$  (center of distribution above), we have the following equation for the  
 590 other two dimensions:

$$\text{imag}(\lambda_1)^2 = a_1 a_4 - a_2 a_3 \quad (15)$$

591 Since we constrained  $E_{q_\theta}[\text{imag}(\lambda)] = 2\pi$  (with  $\omega = 1$ ), we can plot contours of the equation  
 592  $\text{imag}(\lambda_1)^2 = a_1 a_4 - a_2 a_3 = (2\pi)^2$  for various  $a_1 a_4$  (Fig. S3A). If  $\sigma_{1,4} = E_{q_\theta}(|a_1 a_4 - E_{q_\theta}[a_1 a_4]|)$ ,  
 593 then we plot the contours as  $a_1 a_4 = 0$  (black),  $a_1 a_4 = -\sigma_{1,4}$  (black dotted), and  $a_1 a_4 = -2\sigma_{1,4}$   
 594 (grey dotted) (Fig. S3B). This validates the curved structure of the inferred distribution learned  
 595 through EPI. We take steps in negative standard deviation of  $a_1 a_4$  (dotted and gray lines), since  
 596 there are few positive values  $a_1 a_4$  in the posterior. Subtler model-behavior combinations will have  
 597 even more complexity, further motivating the use of EPI for understanding these systems. Indeed,  
 598 we sample a distribution of systems oscillating near 1Hz (Fig. S4).

### 599 A.1.2 Augmented Lagrangian optimization

600 To optimize  $q_\theta(z)$  in equation 1, the constrained optimization is performed using the augmented  
 601 Lagrangian method. The following objective is minimized:

$$L(\theta; \alpha, c) = -H(q_\theta) + \alpha^\top \delta(\theta) + \frac{c}{2} \|\delta(\theta)\|^2 \quad (16)$$

602 where  $\delta(\theta) = E_{z \sim q_\theta} [E_{x \sim p(x|z)} [T(x) - \mu]]$ ,  $\alpha \in \mathcal{R}^m$  are the Lagrange multipliers and  $c$  is the penalty  
 603 coefficient. For a fixed  $(\alpha, c)$ ,  $\theta$  is optimized with stochastic gradient descent. A low value of  $c$  is

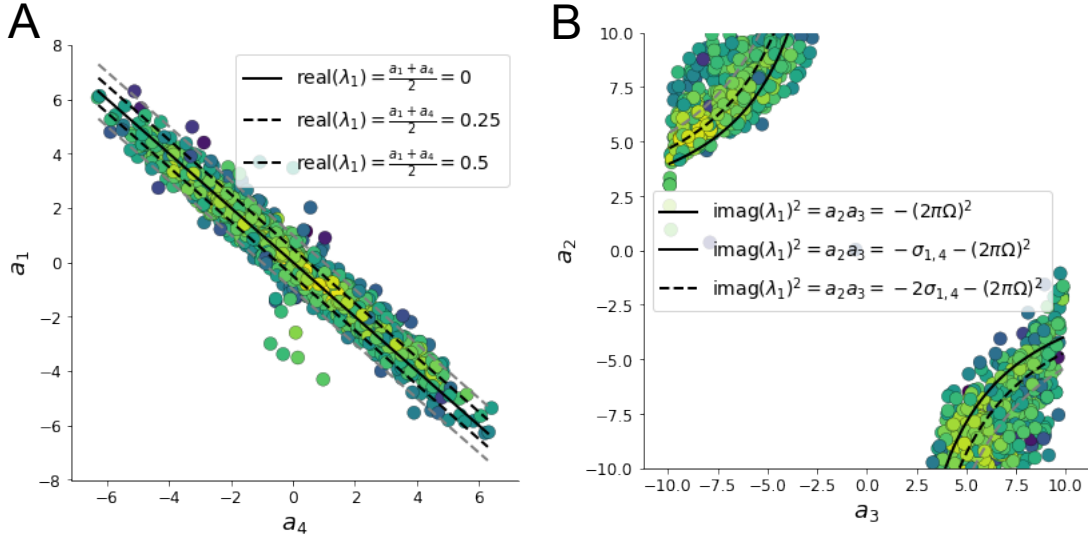


Fig. S3: A. Probability contours in the  $a_1 - a_4$  plane can be derived from the relationship to emergent property statistic of growth/decay factor. B. Probability contours in the  $a_2 - a_3$  plane can be derived from relationship to the emergent property statistic of oscillation frequency.

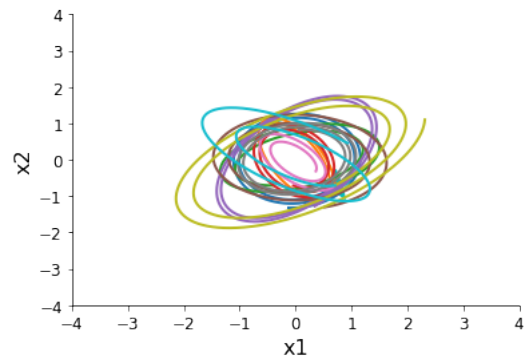


Fig. S4: Sampled dynamical system trajectories from the EPI distribution. Each trajectory is initialized at  $x(0) = \left[ \frac{\sqrt{2}}{2} \quad -\frac{\sqrt{2}}{2} \right]$ .

604 used initially, and increased during each augmented Lagrangian epoch – a period of optimization  
 605 with fixed  $\alpha$  and  $c$  for a given number of stochastic optimization iterations. Similarly,  $\alpha$  is tuned  
 606 each epoch based on the constraint violations. For the linear 2-dimensional system (Fig. S2C)  
 607 optimization hyperparameters are initialized to  $c_1 = 10^{-4}$  and  $\alpha_1 = 0$ . The penalty coefficient  
 608 is updated based on a hypothesis test regarding the reduction in constraint violation. The p-  
 609 value of  $E[|\delta(\theta_{k+1})|] > \gamma E[|\delta(\theta_k)|]$  is computed, and  $c_{k+1}$  is updated to  $\beta c_k$  with probability  
 610  $1 - p$ . Throughout the project,  $\beta = 4.0$  and  $\gamma = 0.25$  is used. The other update rule is  $\alpha_{k+1} =$   
 611  $\alpha_k + c_k \frac{1}{n} \sum_{i=1}^n (T(x^{(i)}) - \mu)$ . In this example, each augmented Lagrangian epoch ran for 2,000  
 612 iterations. We consider the optimization to have converged when a null hypothesis test of constraint  
 613 violations being zero is accepted for all constraints at a significance threshold 0.05. This is the dotted  
 614 line on the plots below depicting the optimization cutoff of EPI optimization for the 2-dimensional  
 615 linear system. If the optimization is left to continue running, entropy usually decreases, and  
 616 structural pathologies in the distribution may be introduced.

617 The intention is that  $c$  and  $\alpha$  start at values encouraging entropic growth early in optimization.  
 618 Then, as they increase in magnitude with each training epoch, the constraint satisfaction terms are  
 619 increasingly weighted, resulting in a decrease in entropy. Rather than using a naive initialization,  
 620 before EPI, we optimize the deep probability distribution parameters to generate samples of an  
 621 isotropic gaussian of a selected variance, such as 1.0 for the 2D LDS example. This provides a  
 622 convenient starting point, whose level of entropy is controlled by the user.

### 623 A.1.3 Normalizing flows

624 Since we are optimizing parameters  $\theta$  of our deep probability distribution with respect to the  
 625 entropy, we will need to take gradients with respect to the log-density of samples from the deep  
 626 probability distribution.

$$H(q_\theta(z)) = \int -q_\theta(z) \log(q_\theta(z)) dz = E_{z \sim q_\theta} [-\log(q_\theta(z))] = E_{\omega \sim q_0} [-\log(q_\theta(f_\theta(\omega)))] \quad (17)$$

$$\nabla_\theta H(q_\theta(z)) = E_{\omega \sim q_0} [-\nabla_\theta \log(q_\theta(f_\theta(\omega)))] \quad (18)$$

628 Deep probability models typically consist of several layers of fully connected neural networks.  
 629 When each neural network layer is restricted to be a bijective function, the sample density can be  
 630 calculated using the change of variables formula at each layer of the network. For  $z' = f(z)$ ,

$$q(z') = q(f^{-1}(z')) \left| \det \frac{\partial f^{-1}(z')}{\partial z'} \right| = q(z) \left| \det \frac{\partial f(z)}{\partial z} \right|^{-1} \quad (19)$$

631 However, this computation has cubic complexity in dimensionality for fully connected layers. By  
 632 restricting our layers to normalizing flows [15] – bijective functions with fast log determinant ja-  
 633 cobian computations, we can tractably optimize deep generative models with objectives that are a  
 634 function of sample density, like entropy. Most of our analyses use real NVP [50], which have proven  
 635 effective in our architecture searches, and have the advantageous features of fast sampling and fast  
 636 density evaluation.

637 **A.1.4 Related work**

638 (To come)

639

640 **A.1.5 Emergent property inference as variational inference in an exponential family**

641 (To come)

642

643 **A.2 Theoretical models**

644 In this study, we used emergent property inference to examine several models relevant to theoretical  
 645 neuroscience. Here, we provide the details of each model and the related analyses.

646 **A.2.1 Stomatogastric ganglion**

647 Each neuron's membrane potential  $x_m(t)$  is the solution of the following differential equation.

$$C_m \frac{\partial x_m}{\partial t} = -[h_{leak}(x; z) + h_{Ca}(x; z) + h_K(x; z) + h_{hyp}(x; z) + h_{elec}(x; z) + h_{syn}(x; z)] \quad (20)$$

648 The membrane potential of each neuron is affected by the leak, calcium, potassium, hyperpolariza-  
 649 tion, electrical and synaptic currents, respectively. The capacitance of the cell membrane was set to  
 650  $C_m = 1nF$ . Each current is a function of the neuron's membrane potential  $x_m$  and the parameters  
 651 of the circuit such as  $g_{el}$  and  $g_{syn}$ , whose effect on the circuit is considered in the motivational

example of EPI in Fig. 1. Specifically, the currents are the difference in the neuron's membrane potential and that current type's reversal potential multiplied by a conductance:

$$h_{leak}(x; z) = g_{leak}(x_m - V_{leak}) \quad (21)$$

$$h_{elec}(x; z) = g_{el}(x_m^{post} - x_m^{pre}) \quad (22)$$

$$h_{syn}(x; z) = g_{syn}S_\infty^{pre}(x_m^{post} - V_{syn}) \quad (23)$$

$$h_{Ca}(x; z) = g_{Ca}M_\infty(x_m - V_{Ca}) \quad (24)$$

$$h_K(x; z) = g_KN(x_m - V_K) \quad (25)$$

$$h_{hyp}(x; z) = g_hH(x_m - V_{hyp}) \quad (26)$$

The reversal potentials were set to  $V_{leak} = -40mV$ ,  $V_{Ca} = 100mV$ ,  $V_K = -80mV$ ,  $V_{hyp} = -20mV$ , and  $V_{syn} = -75mV$ . The other conductance parameters were fixed to  $g_{leak} = 1 \times 10^{-4}\mu S$ .  $g_{Ca}$ ,  $g_K$ , and  $g_{hyp}$  had different values based on fast, intermediate (hub) or slow neuron. Fast:  $g_{Ca} = 1.9 \times 10^{-2}$ ,  $g_K = 3.9 \times 10^{-2}$ , and  $g_{hyp} = 2.5 \times 10^{-2}$ . Intermediate:  $g_{Ca} = 1.7 \times 10^{-2}$ ,  $g_K = 1.9 \times 10^{-2}$ , and  $g_{hyp} = 8.0 \times 10^{-3}$ . Intermediate:  $g_{Ca} = 8.5 \times 10^{-3}$ ,  $g_K = 1.5 \times 10^{-2}$ , and  $g_{hyp} = 1.0 \times 10^{-2}$ .

Furthermore, the Calcium, Potassium, and hyperpolarization channels have time-dependent gating dynamics dependent on steady-state gating variables  $M_\infty$ ,  $N_\infty$  and  $H_\infty$ , respectively.

$$M_\infty = 0.5 \left( 1 + \tanh \left( \frac{x_m - v_1}{v_2} \right) \right) \quad (27)$$

$$\frac{\partial N}{\partial t} = \lambda_N(N_\infty - N) \quad (28)$$

$$N_\infty = 0.5 \left( 1 + \tanh \left( \frac{x_m - v_3}{v_4} \right) \right) \quad (29)$$

$$\lambda_N = \phi_N \cosh \left( \frac{x_m - v_3}{2v_4} \right) \quad (30)$$

$$\frac{\partial H}{\partial t} = \frac{(H_\infty - H)}{\tau_h} \quad (31)$$

$$H_\infty = \frac{1}{1 + \exp \left( \frac{x_m + v_5}{v_6} \right)} \quad (32)$$

$$\tau_h = 272 - \left( \frac{-1499}{1 + \exp \left( \frac{-x_m + v_7}{v_8} \right)} \right) \quad (33)$$

where we set  $v_1 = 0mV$ ,  $v_2 = 20mV$ ,  $v_3 = 0mV$ ,  $v_4 = 15mV$ ,  $v_5 = 78.3mV$ ,  $v_6 = 10.5mV$ ,  $v_7 = -42.2mV$ ,  $v_8 = 87.3mV$ ,  $v_9 = 5mV$ , and  $v_{th} = -25mV$ . These are the same parameter values used in [20].

675 Finally, there is a synaptic gating variable as well:

$$S_\infty = \frac{1}{1 + \exp\left(\frac{v_{th} - x_m}{v_0}\right)} \quad (34)$$

676 When the dynamic gating variables are considered, this is actually a 15-dimensional nonlinear  
677 dynamical system.

678 In order to measure the frequency of the hub neuron during EPI, the STG model was simulated  
679 for  $T = 500$  time steps of  $dt = 25ms$ . In EPI, since gradients are taken through the simulation  
680 process, the number of time steps are kept as modest if possible. The chosen  $dt$  and  $T$  were the  
681 most computationally convenient choices yielding accurate frequency measurement.

682 Our original approach to measuring frequency was to take the max of the fast Fourier transform  
683 (FFT) of the simulated time series. There are a few key considerations here. One is resolution  
684 in frequency space. Each FFT entry will correspond to a signal frequency of  $\frac{F_s k}{N}$ , where  $N$  is  
685 the number of samples used for the FFT,  $F_s = \frac{1}{dt}$ , and  $k \in [0, 1, \dots, N - 1]$ . Our resolution is  
686 improved by increasing  $N$  and decreasing  $dt$ . Increasing  $N = T - b$ , where  $b$  is some fixed number  
687 of buffer burn-in initialization samples, necessitates an increase in simulation time steps  $T$ , which  
688 directly increases computational cost. Increasing  $F_s$  (decreasing  $dt$ ) increases system approximation  
689 accuracy, but requires more time steps before a full cycle is observed. At the level of  $dt = 0.025$ ,  
690 thousands of temporal samples were required for resolution of .01Hz. These challenges in frequency  
691 resolution with the discrete Fourier transform motivated the use of an alternative basis of complex  
692 exponentials. Instead, we used a basis of complex exponentials with frequencies from 0.0-1.0 Hz at  
693 0.01Hz resolution,  $\Phi = [0.0, 0.01, \dots, 1.0]^\top$

694 Another consideration was that the frequency spectra of the hub neuron has several peaks. This  
695 was due to high-frequency sub-threshold activity. The maximum frequency was often not the firing  
696 frequency. Accordingly, subthreshold activity was set to zero, and the whole signal was low-pass  
697 filtered with a moving average window of length 20. The signal was subsequently mean centered.  
698 After this pre-processing, the maximum frequency in the filter bank accurately reflected the firing  
699 frequency.

700 Finally, to differentiate through the maximum frequency identification step, we used a sum-of-  
701 powers normalization strategy: Let  $\mathcal{X}_i \in \mathcal{C}^{|\Phi|}$  be the complex exponential filter bank dot products  
702 with the signal  $x_i \in \mathcal{R}^N$ , where  $i \in \{\text{f1}, \text{f2}, \text{hub}, \text{s1}, \text{s2}\}$ . The “frequency identification” vector is

$$u_i = \frac{|\mathcal{X}_i|^\alpha}{\sum_{k=1}^N |\mathcal{X}_i(k)|^\alpha} \quad (35)$$

703 The frequency is then calculated as  $\Omega_i = u_i^\top \Phi$  with  $\alpha = 100$ .

704 Network syncing, like all other emergent properties in this work, are defined by the emergent  
 705 property statistics and values. The emergent property statistics are the first- and second-moments  
 706 of the firing frequencies. The first moments are set to 0.55Hz, while the second moments are set to  
 707 0.025Hz<sup>2</sup>.

$$E \begin{bmatrix} \Omega_{f1} \\ \Omega_{f2} \\ \Omega_{hub} \\ \Omega_{s1} \\ \Omega_{s2} \\ (\Omega_{f1} - 0.55)^2 \\ (\Omega_{f2} - 0.55)^2 \\ (\Omega_{hub} - 0.55)^2 \\ (\Omega_{s1} - 0.55)^2 \\ (\Omega_{s2} - 0.55)^2 \end{bmatrix} = \begin{bmatrix} 0.55 \\ 0.55 \\ 0.55 \\ 0.55 \\ 0.55 \\ 0.025^2 \\ 0.025^2 \\ 0.025^2 \\ 0.025^2 \\ 0.025^2 \end{bmatrix} \quad (36)$$

708 For EPI in Fig 2C, we used a real NVP architecture with two coupling layers. Each coupling layer  
 709 had two hidden layers of 10 units each, and we mapped onto a support of  $z \in \left[ \begin{bmatrix} 0 \\ 0 \end{bmatrix}, \begin{bmatrix} 10 \\ 8 \end{bmatrix} \right]$ . We  
 710 have shown the EPI optimization that converged with maximum entropy across 2 random seeds  
 711 and augmented Lagrangian coefficient initializations of  $c_0=0$ , 2, and 5.

712 **A.2.2 Primary visual cortex**

713 The dynamics of each neural populations average rate  $x = \begin{bmatrix} x_E \\ x_P \\ x_S \\ x_V \end{bmatrix}$  are given by:

$$\tau \frac{dx}{dt} = -x + [Wx + h]_+^n \quad (37)$$

714 Some neuron-types largely lack synaptic projections to other neuron-types [52], and it is popular

715 to only consider a subset of the effective connectivities [21].

$$W = \begin{bmatrix} W_{EE} & W_{EP} & W_{ES} & 0 \\ W_{PE} & W_{PP} & W_{PS} & 0 \\ W_{SE} & 0 & 0 & W_{SV} \\ W_{VE} & W_{VP} & W_{VS} & 0 \end{bmatrix} \quad (38)$$

716 Estimates of the probability of connection and strength of connection from the Allen institute  
 717 result in an estimate of the effective connectivity [?]:

$$W = \begin{bmatrix} 0.0576 & 0.19728 & 0.13144 & 0 \\ 0.58855 & 0.30668 & 0.4285 & 0 \\ 0.15652 & 0 & 0 & 0.2 \\ 0.13755 & 0.0902 & 0.4004 & 0 \end{bmatrix} \quad (39)$$

718 We look at how this four-dimensional nonlinear dynamical model of V1 responds to different inputs,  
 719 and compare the predictions of the linear response to the approximate posteriors obtained through  
 720 EPI. The input to the system is the sum of a baseline input  $b = [1 \ 1 \ 1 \ 1]^\top$  and a differential  
 721 input  $dh$ :

$$h = b + dh \quad (40)$$

722 All simulations of this system had  $T = 100$  time points, a time step  $dt = 5\text{ms}$ , and time constant  
 723  $\tau = 20\text{ms}$ . And the system was initialized to a random draw  $x(0)_i \sim \mathcal{N}(1, 0.01)$ .

724 We can describe the dynamics of this system more generally by

$$\dot{x}_i = -x_i + f(u_i) \quad (41)$$

725 where the input to each neuron is

$$u_i = \sum_j W_{ij} x_j + h_i \quad (42)$$

726 Let  $F_{ij} = \gamma_i \delta(i, j)$ , where  $\gamma_i = f'(u_i)$ . Then, the linear response is

$$\frac{\partial x_{ss}}{\partial h} = F(W \frac{\partial x_{ss}}{\partial h} + I) \quad (43)$$

727 which is calculable by

$$\frac{\partial x_{ss}}{\partial h} = (F^{-1} - W)^{-1} \quad (44)$$

728 The emergent property we considered was the first and second moments of the change in rate  $dx$   
 729 between the baseline input  $h = b$  and  $h = b + dh$ . We use the following notation to indicate that

730 the emergent property statistics were set to the following values:

$$\mathcal{B}(\alpha, y) \leftrightarrow E \begin{bmatrix} dx_{\alpha,ss} \\ (dx_{\alpha,ss} - y)^2 \end{bmatrix} = \begin{bmatrix} y \\ 0.01^2 \end{bmatrix} \quad (45)$$

731 In the final analysis for this model, we sweep the input one neuron at a time away from the mode  
 732 of each inferred distributions  $dh^* = z^* = \text{argmax}_z \log q_\theta(z | \mathcal{B}(\alpha, 0.1))$ . The differential responses  
 733  $dx_{\alpha,ss}$  are examined at perturbed inputs  $h = b + dh^* + \Delta h_\alpha u_\alpha$  where  $u_\alpha$  is a unit vector in the  
 734 dimension of  $\alpha$  and  $\Delta h_\alpha \in [-15, 15]$ .

735 For each  $\mathcal{B}(\alpha, y)$  with  $\alpha \in \{E, P, S, V\}$  and  $y \in \{0.1, 0.5\}$ , we ran EPI with five different random  
 736 initial seeds using an architecture of four coupling layers, each with two hidden layers of 10 units.  
 737 We set  $c_0 = 10^5$ . The support of the learned distribution was restricted to  $z_i \in [-5, 5]$ .

738 **A.2.3 Superior colliculus**

739 There are four total units: two in each hemisphere corresponding to the Pro/contralateral and  
 740 Anti/ipsilateral populations. Each unit has an activity ( $x_i$ ) and internal variable ( $u_i$ ) related by

$$x_i(t) = \left( \frac{1}{2} \tanh \left( \frac{v_i(t) - \epsilon}{\zeta} \right) + \frac{1}{2} \right) \quad (46)$$

741  $\epsilon = 0.05$  and  $\zeta = 0.5$  control the position and shape of the nonlinearity, respectively.

742 We can order the elements of  $x_i$  and  $v_i$  into vectors  $x$  and  $v$  with elements

$$x = \begin{bmatrix} x_{LP} \\ x_{LA} \\ x_{RP} \\ x_{RA} \end{bmatrix} \quad v = \begin{bmatrix} v_{LP} \\ v_{LA} \\ v_{RP} \\ v_{RA} \end{bmatrix} \quad (47)$$

743 The internal variables follow dynamics:

$$\tau \frac{\partial v}{\partial t} = -v + Wx + h + \sigma \partial B \quad (48)$$

744 with time constant  $\tau = 0.09s$  and gaussian noise  $\sigma \partial B$  controlled by the magnitude of  $\sigma = 1.0$ . The  
 745 weight matrix has 8 parameters  $sW_P$ ,  $sW_A$ ,  $vW_{PA}$ ,  $vW_{AP}$ ,  $hW_P$ ,  $hW_A$ ,  $dW_{PA}$ , and  $dW_{AP}$  (Fig.  
 746 4B).

$$W = \begin{bmatrix} sW_P & vW_{PA} & hW_P & dW_{PA} \\ vW_{AP} & sW_A & dW_{AP} & hW_A \\ hW_P & dW_{PA} & sW_P & vW_{PA} \\ dW_{AP} & hW_A & vW_{AP} & sW_A \end{bmatrix} \quad (49)$$

<sup>747</sup> The system receives five inputs throughout each trial, which has a total length of 1.8s.

$$h = h_{\text{rule}} + h_{\text{choice-period}} + h_{\text{light}} \quad (50)$$

<sup>748</sup> There are rule-based inputs depending on the condition,

$$h_{P,\text{rule}}(t) = \begin{cases} I_{P,\text{rule}} \begin{bmatrix} 1 & 0 & 0 & 1 \end{bmatrix}^\top, & \text{if } t \leq 1.2s \\ 0, & \text{otherwise} \end{cases} \quad (51)$$

<sup>749</sup>

$$h_{A,\text{rule}}(t) = \begin{cases} I_{A,\text{rule}} \begin{bmatrix} 0 & 1 & 1 & 0 \end{bmatrix}^\top, & \text{if } t \leq 1.2s \\ 0, & \text{otherwise} \end{cases} \quad (52)$$

<sup>750</sup> a choice-period input,

$$h_{\text{choice}}(t) = \begin{cases} I_{\text{choice}} \begin{bmatrix} 1 & 1 & 1 & 1 \end{bmatrix}^\top, & \text{if } t > 1.2s \\ 0, & \text{otherwise} \end{cases} \quad (53)$$

<sup>751</sup> and an input to the right or left-side depending on where the light stimulus is delivered.

$$h_{\text{light}}(t) = \begin{cases} I_{\text{light}} \begin{bmatrix} 1 & 1 & 0 & 0 \end{bmatrix}^\top, & \text{if } t > 1.2s \text{ and Left} \\ I_{\text{light}} \begin{bmatrix} 0 & 0 & 1 & 1 \end{bmatrix}^\top, & \text{if } t > 1.2s \text{ and Right} \\ 0, & t \leq 1.2s \end{cases} \quad (54)$$

<sup>752</sup> The input parameterization was fixed to  $I_{P,\text{rule}} = 10$ ,  $I_{A,\text{rule}} = 10$ ,  $I_{\text{choice}} = 2$ , and  $I_{\text{light}} = 1$

<sup>753</sup> To produce a Bernoulli rate of  $p_{LP}$  in the Left, Pro condition (we can generalize this to either cue,

<sup>754</sup> or stimulus condition), let  $\hat{p}_i$  be the empirical average steady state (ss) response (final  $x_{LP}$  at end

<sup>755</sup> of task) over M=500 gaussian noise draws for a given SC model parameterization  $z_i$ :

$$\hat{p}_i = E_{\sigma \partial B} [x_{LP,ss} | s = L, c = P, z_i] = \frac{1}{M} \sum_{j=1}^M x_{LP,ss}(s = L, c = P, z_i, \sigma \partial B_j) \quad (55)$$

<sup>756</sup> For the first constraint, the average over posterior samples (from  $q_\theta(z)$ ) to be  $p_{LP}$ :

$$E_{z_i \sim q_\phi} [E_{\sigma \partial B} [x_{LP,ss} | s = L, c = P, z_i]] = E_{z_i \sim q_\phi} [\hat{p}_i] = p_{LP} \quad (56)$$

<sup>757</sup> We can then ask that the variance of the steady state responses across gaussian draws, is the

<sup>758</sup> Bernoulli variance for the empirical rate  $\hat{p}_i$ .

$$E_{z \sim q_\phi} [\sigma_{err}^2] = 0 \quad (57)$$

759

$$\sigma_{err}^2 = \text{Var}_{\sigma \partial B} [x_{LP,ss} \mid s = L, c = P, z_i] - \hat{p}_i(1 - \hat{p}_i) \quad (58)$$

760 We have an additional constraint that the Pro neuron on the opposite hemisphere should have the  
 761 opposite value. We can enforce this with a final constraint:

$$E_{z \sim q_\phi} [d_P] = 1 \quad (59)$$

762

$$E_{\sigma \partial W} [(x_{LP,ss} - x_{RP,ss})^2 \mid s = L, c = P, z_i] \quad (60)$$

763 We refer to networks obeying these constraints as Bernoulli, winner-take-all networks. Since the  
 764 maximum variance of a random variable bounded from 0 to 1 is the Bernoulli variance ( $\hat{p}(1 - \hat{p})$ ),  
 765 and the maximum squared difference between two variables bounded from 0 to 1 is 1, we do not  
 766 need to control the second moment of these test statistics. In reality, these variables are dynamical  
 767 system states and can only exponentially decay (or saturate) to 0 (or 1), so the Bernoulli variance  
 768 error and squared difference constraints can only be undershot. This is important to be mindful  
 769 of when evaluating the convergence criteria. Instead of using our usual hypothesis testing criteria  
 770 for convergence to the emergent property, we set a slack variable threshold for these technically  
 771 infeasible constraints to 0.05.

772 Training DSNs to learn distributions of dynamical system parameterizations that produce Bernoulli  
 773 responses at a given rate (with small variance around that rate) was harder to do than expected.  
 774 There is a pathology in this optimization setup, where the learned distribution of weights is bimodal  
 775 attributing a fraction  $p$  of the samples to an expansive mode (which always sends  $x_{LP}$  to 1), and a  
 776 fraction  $1 - p$  to a decaying mode (which always sends  $x_{LP}$  to 0). This pathology was avoided using  
 777 an inequality constraint prohibiting parameter samples that resulted in low variance of responses  
 778 across noise.

779 In total, the emergent property of rapid task switching accuracy at level  $p$  was defined as

$$\mathcal{B}(p) \leftrightarrow \begin{bmatrix} \hat{p}_P \\ \hat{p}_A \\ (\hat{p}_P - p)^2 \\ (\hat{p}_A - p)^2 \\ \sigma_{P,err}^2 \\ \sigma_{A,err}^2 \\ d_P \\ d_A \end{bmatrix} = \begin{bmatrix} p \\ p \\ 0.15^2 \\ 0.15^2 \\ 0 \\ 0 \\ 1 \\ 1 \end{bmatrix} \quad (61)$$

780 For each accuracy level  $p$ , we ran EPI for 10 different random seeds and selected the maximum  
 781 entropy solution using an architecture of 10 planar flows with  $c_0 = 2$ . The support of  $z$  was  $\mathcal{R}^8$ .

782 **A.2.4 Rank-1 RNN**

783 The network dynamics of neuron  $i$ 's rate  $x$  evolve according to:

$$\dot{x}_i(t) = -x_i(t) + \sum_{j=1}^N J_{ij}\phi(x_j(t)) + I_i \quad (62)$$

784 where the connectivity is comprised of a random and structured component:

$$J_{ij} = g\chi_{ij} + P_{ij} \quad (63)$$

785 The random all-to-all component has elements drawn from  $\chi_{ij} \sim \mathcal{N}(0, \frac{1}{N})$ , and the structured  
 786 component is a sum of  $r$  unit rank terms:

$$P_{ij} = \sum_{k=1}^r \frac{m_i^{(k)} n_j^{(k)}}{N} \quad (64)$$

787 We use this theory to compute  $T(x)$  when running EPI.

788 Rank-1 vectors  $m$  and  $n$  have elements drawn

$$m_i \sim \mathcal{N}(M_m, \Sigma_m)$$

789

$$n_i \sim \mathcal{N}(M_n, \Sigma_n)$$

790 The current has the following statistics:

$$I = M_I + \frac{\Sigma_{mI}}{\Sigma_m} x_1 + \frac{\Sigma_{nI}}{\Sigma_n} x_2 + \Sigma_\perp h$$

791 where  $x_1$ ,  $x_2$ , and  $h$  are standard normal random variables.

792 The  $\ddot{\Delta}$  equation is broken into the equation for  $\Delta_0$  and  $\Delta_\infty$  by the autocorrelation dynamics  
 793 assertions.

$$\Delta(\tau) = -\frac{\partial V}{\partial \Delta}$$

794

$$\ddot{\Delta} = \Delta - \{g^2 \langle [\phi_i(t)\phi_i(t+\tau)] \rangle + \Sigma_m^2 \kappa^2 + 2\Sigma_{mI} \kappa + \Sigma_I^2\}$$

795 We can write out the potential function by integrating the negated RHS.

$$V(\Delta, \Delta_0) = \int \mathcal{D}\Delta \frac{\partial V(\Delta, \Delta_0)}{\partial \Delta}$$

796

$$V(\Delta, \Delta_0) = -\frac{\Delta^2}{2} + g^2 \langle [\Phi_i(t)\Phi_i(t+\tau)] \rangle + (\Sigma_m^2 \kappa^2 + 2\Sigma_{mI}\kappa + \Sigma_I^2)\Delta + C$$

797 We assume that as time goes to infinity, the potential relaxes to a steady state.

$$\frac{\partial V(\Delta_\infty, \Delta_0)}{\partial \Delta} = 0$$

798

$$\frac{\partial V(\Delta_\infty, \Delta_0)}{\partial \Delta} = -\Delta + \{g^2 \langle [\phi_i(t)\phi_i(t+\infty)] \rangle + \Sigma_m^2 \kappa^2 + 2\Sigma_{mI}\kappa + \Sigma_I^2\} = 0$$

799

$$\Delta_\infty = g^2 \langle [\phi_i(t)\phi_i(t+\infty)] \rangle + \Sigma_m^2 \kappa^2 + 2\Sigma_{mI}\kappa + \Sigma_I^2$$

800

$$\Delta_\infty = g^2 \int \mathcal{D}z \left[ \int \mathcal{D}x \phi(\mu + \sqrt{\Delta_0 - \Delta_\infty}x + \sqrt{\Delta_\infty}z) \right]^2 + \Sigma_m^2 \kappa^2 + 2\Sigma_{mI}\kappa + \Sigma_I^2$$

801 Also, we assume that the energy of the system is preserved throughout the entirety of its evolution.

$$V(\Delta_0, \Delta_0) = V(\Delta_\infty, \Delta_0)$$

802

$$-\frac{\Delta_0^2}{2} + g^2 \langle [\Phi_i(t)\Phi_i(t)] \rangle + (\Sigma_m^2 \kappa^2 + 2\Sigma_{mI}\kappa + \Sigma_I^2)\Delta_0 + C = -\frac{\Delta_\infty^2}{2} + g^2 \langle [\Phi_i(t)\Phi_i(t)] \rangle + (\Sigma_m^2 \kappa^2 + 2\Sigma_{mI}\kappa + \Sigma_I^2)\Delta_\infty + C$$

803

$$\frac{\Delta_0^2 - \Delta_\infty^2}{2} = g^2 (\langle [\Phi_i(t)\Phi_i(t)] \rangle - \langle [\Phi_i(t)\Phi_i(t)] \rangle) + (\Sigma_m^2 \kappa^2 + 2\Sigma_{mI}\kappa + \Sigma_I^2)(\Delta_0 - \Delta_\infty)$$

804

$$\begin{aligned} \frac{\Delta_0^2 - \Delta_\infty^2}{2} &= g^2 \left( \int \mathcal{D}z \Phi^2(\mu + \sqrt{\Delta_0}z) - \int \mathcal{D}z \int \mathcal{D}x \Phi(\mu + \sqrt{\Delta_0 - \Delta_\infty}x + \sqrt{\Delta_\infty}z) \right) \\ &\quad + (\Sigma_m^2 \kappa^2 + 2\Sigma_{mI}\kappa + \Sigma_I^2)(\Delta_0 - \Delta_\infty) \end{aligned}$$

805 **Consistency equations:**

806

$$\begin{aligned} \mu &= F(\mu, \kappa, \Delta_0, \Delta_\infty) = M_m \kappa + M_I \\ \kappa &= G(\mu, \kappa, \Delta_0, \Delta_\infty) = M_n \langle [\phi_i] \rangle + \Sigma_{nI} \langle [\phi'_i] \rangle \\ \frac{\Delta_0^2 - \Delta_\infty^2}{2} &= H(\mu, \kappa, \Delta_0, \Delta_\infty) = g^2 \left( \int \mathcal{D}z \Phi^2(\mu + \sqrt{\Delta_0}z) - \int \mathcal{D}z \int \mathcal{D}x \Phi(\mu + \sqrt{\Delta_0 - \Delta_\infty}x + \sqrt{\Delta_\infty}z) \right) \\ &\quad + (\Sigma_m^2 \kappa^2 + 2\Sigma_{mI}\kappa + \Sigma_I^2)(\Delta_0 - \Delta_\infty) \\ \Delta_\infty &= L(\mu, \kappa, \Delta_0, \Delta_\infty) = g^2 \int \mathcal{D}z \left[ \int \mathcal{D}x \phi(\mu + \sqrt{\Delta_0 - \Delta_\infty}x + \sqrt{\Delta_\infty}z) \right]^2 + \Sigma_m^2 \kappa^2 + 2\Sigma_{mI}\kappa + \Sigma_I^2 \end{aligned} \tag{65}$$

807 We can solve these equations by simulating the following Langevin dynamical system.

$$\begin{aligned}
 x(t) &= \frac{\Delta_0(t)^2 - \Delta_\infty(t)^2}{2} \\
 \Delta_0(t) &= \sqrt{2x(t) + \Delta_\infty(t)^2} \\
 \dot{\mu}(t) &= -\mu(t) + F(\mu(t), \kappa(t), \Delta_0(t), \Delta_\infty(t)) \\
 \dot{\kappa}(t) &= -\kappa + G(\mu(t), \kappa(t), \Delta_0(t), \Delta_\infty(t)) \\
 \dot{x}(t) &= -x(t) + H(\mu(t), \kappa(t), \Delta_0(t), \Delta_\infty(t)) \\
 \dot{\Delta_\infty}(t) &= -\Delta_\infty(t) + L(\mu(t), \kappa(t), \Delta_0(t), \Delta_\infty(t))
 \end{aligned} \tag{66}$$

808 Then, the temporal variance is simply calculated via

$$\Delta_T = \Delta_0 - \Delta_\infty \tag{67}$$

809 **A.3 Supplementary Figures**

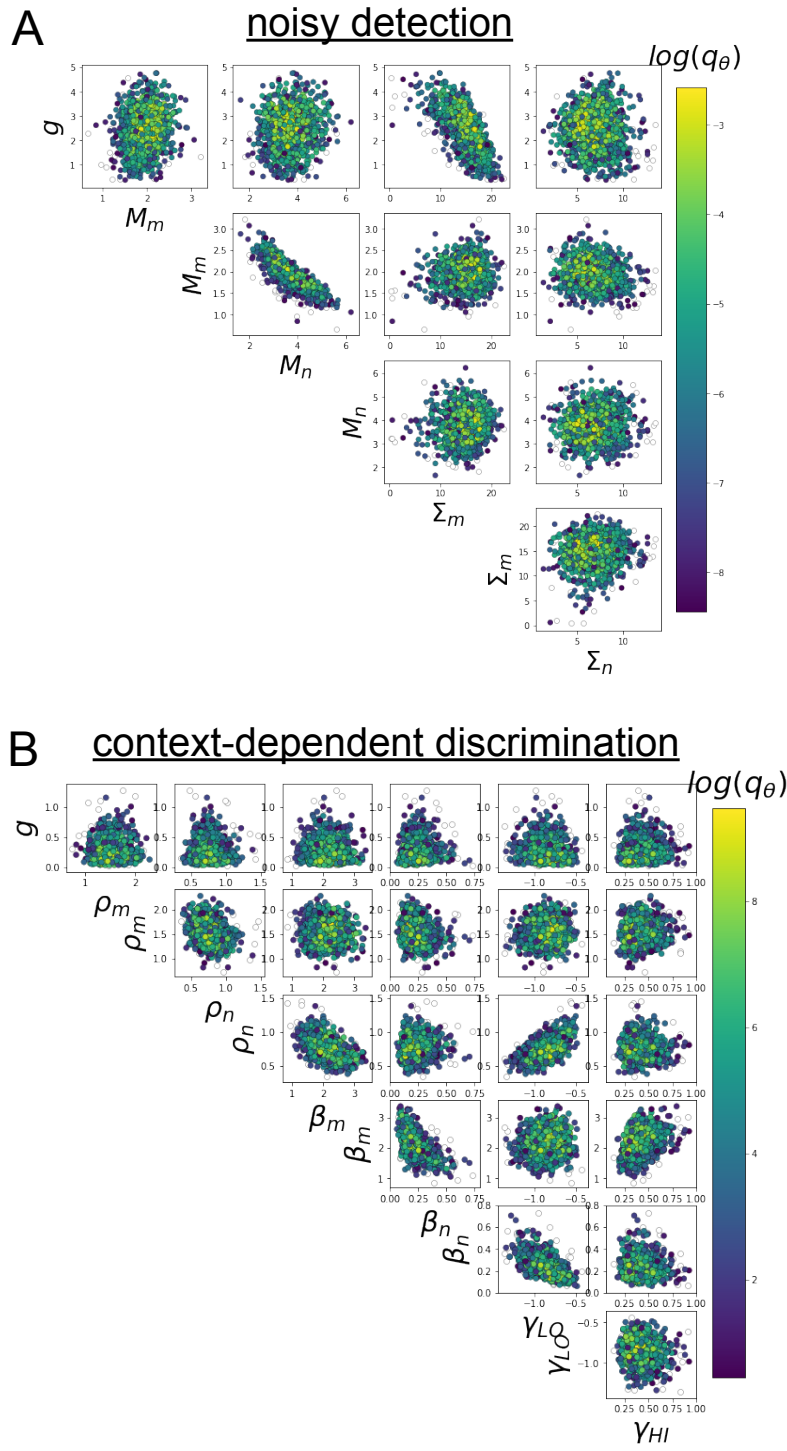


Fig. S1: A. EPI for rank-1 networks doing discrimination. B. EPI for rank-2 networks doing context-dependent discrimination.